RSC Advances

PAPER

View Article Online
View Journal | View Issue

Cite this: *RSC Adv.*, 2026, **16**, 13162

Machine learning-enhanced novel design and performance optimization of M_3SbI_3 (M = Ba and Ca) based dual absorber perovskite solar cells

Md. Anwer Hossain,[a] Md Rasidul Islam, *[bc] A. M. Quraishi,[d] Sobhi M. Gomha, [e] Magdi E. A. Zaki[f] and Md Masud Rana*[c]

The growing demand for renewable energy necessitates the development of sustainable, high-performance, eco-conscious solar cells. This research proposes a novel lead-free dual-absorber perovskite solar cell (DAPSC) utilizing Ca_3SbI_3 as the top absorber and Ba_3SbI_3 as the bottom absorber layer. The device structure, Al/FTO/SnS_2/Ca_3SbI_3/Ba_3SbI_3/CBTS/Au, was analyzed by employing SCAPS-1D to evaluate photovoltaic performance under standard AM1.5G illumination. The dual-absorber configuration exhibited a considerably improved power conversion efficiency (PCE) of 36.03%, short-circuit current density (J_{sc}) of 32.18 mA cm^{-2}, open-circuit voltage (V_{oc}) of 1.305 V, and fill factor (FF) of 85.84%, outperforming single-absorber perovskite solar cells. We further employed a Random Forest Regression (RFR) model to forecast the proposed device performance. We found that the machine learning (ML) model achieved excellent predictive performance with an average coefficient of determination (R^2) of 0.9635, mean absolute error (MAE) of 0.4506, and root mean square error (RMSE) of 0.6253. Moreover, feature importance analysis validated by SHAP (Shapley Additive exPlanations) summary plots and correlation matrices revealed that operating temperature and absorber layer parameters (doping, thickness, and defect level) were the most critical factors influencing photovoltaic performance, while electron and hole transport layer properties also played significant roles. These outcomes reveal that the proposed lead-free DAPSC model presents enhanced performance, stability, and environmental compatibility for photovoltaic applications.

Received 19th January 2026
Accepted 3rd March 2026

DOI: 10.1039/d6ra00497k

rsc.li/rsc-advances

1. Introduction

Since global energy demand has increased and non-renewable resources have declined steeply, the search for alternative, reliable renewable energy sources has intensified. Among various renewable energy resources such as tidal, bio-based, ocean, hydro, geothermal, and wind energy, solar energy is evolving because of its reliability, durability, and minimal environmental impact.[1–4] Although silicon-based solar cells drive the photovoltaic market, their performance is approaching theoretical limits, and their reliance on rigid, costly fabrication techniques restricts flexible and emerging applications.[5–7] Despite notable progress in conventional solar cell materials like Si, CdTe, CIGS, GaAs, Sb_2Se_3, CMTS, and $FeSi_2$, PSCs have quickly gained attention for their outstanding photo-electronic performance, reaching single-junction efficiencies surpassing 27% and challenging traditional silicon-based technologies.[8–12] Perovskite materials can harvest a higher number of photons than conventional semiconductors even when the absorber layer (AL) is thinner than 1000 nm.[13,14] Among organic–inorganic perovskites, the most widely studied compositions are represented by the general formula $MABX_3$, which denotes materials with a distinctive crystal structure where MA refers to the methylammonium cation ($CH_3NH_3^+$), B reflects a divalent metal cation like tin (Sn) or lead (Pb) and X corresponds to a halide anion, commonly iodine (I), bromine (Br) or chlorine (Cl).[15–17] Since 2009, inorganic perovskite solar cells (IOPSC) have attracted major focus because of their impressive electronic properties.[18,19]

PSCs have demonstrated notable efficiencies, including 26.7% for $MAPbI_3$ (ref. 20 and 21) and 17.42% for $MAPbBr_3$,[22] while lead-free alternatives such as $MASnBr_3$ and $MASnI_3$ have been reported with power conversion efficiencies of 31.97% and 31.51% respectively.[23,24] Many PSCs still rely on lead, and the

[a]*Department of Electrical and Electronic Engineering, University of Dhaka, Dhaka 1000, Bangladesh*

[b]*Department of Electrical and Electronic Engineering, Jamalpur Science & Technology University, Jamalpur-2012, Bangladesh. E-mail: rasidul@jstu.ac.bd*

[c]*Department of Electrical and Computer Engineering, The University of Texas at Tyler, Tyler 75799, TX, USA. E-mail: mrana@uttyler.edu*

[d]*Department of Electrical Engineering, College of Engineering, Qassim University, Buraydah 51452, Saudi Arabia*

[e]*Department of Chemistry, Faculty of Science, Islamic University of Madinah, Madinah, Saudi Arabia*

[f]*Department of Chemistry, Faculty of Science, Imam Mohammad Ibn Saud Islamic University (IMSIU), Riyadh 11623, Saudi Arabia*

environmental and stability concerns associated with it have encouraged research into safer lead-free PSCs (LFPSCs) that combine strong light absorption, high defect tolerance, suitable band gaps, robust mechanical stability, and favorable electron–hole mobility, making them promising for photovoltaic applications.[25–28] Perovskites of the A_3BX_3 family, A as larger inorganic cation, B as smaller metal cation, and X as anion, have shown great promise for solar energy harvesting, with reported Pb-free PSC efficiencies of 28% (Sr_3SbI_3),[29] 28.15% (Sr_3PI_3),[30] 13.52% (Ca_3AsBr_3) and 22.47% (Ca_3PI_3),[31] 31.7% (Mg_3AsBr_3),[32] 20.87% (Ca_3SbI_3)[33] and 30.49% (Ba_3SbI_3).[34]

The bandgap of a single absorber limits the range of sunlight it can capture, allowing low-energy photons to pass through and high-energy photons to lose excess energy as heat, which constrains efficiency below the Shockley–Queisser theoretical maximum.[35] To overcome this limitation, we investigated a novel dual absorber perovskite solar cell (DAPSC) using Ca_3SbI_3 as the top absorber and Ba_3SbI_3 as the bottom absorber, offering a lead-free alternative with improved environmental safety and enhanced stability. A detailed study integrating simulation and machine learning (ML) for Ca_3SbI_3/Ba_3SbI_3-based inorganic lead-free dual-absorber PSC has not yet been reported, establishing this combined framework as a vital step toward next-generation photovoltaic development.

In this study, we present a novel Ca_3SbI_3/Ba_3SbI_3-based lead-free DAPSC design, incorporating SCAPS-1D simulations in combination with an RFR-based ML model. Single absorber simulations indicate that each material can independently

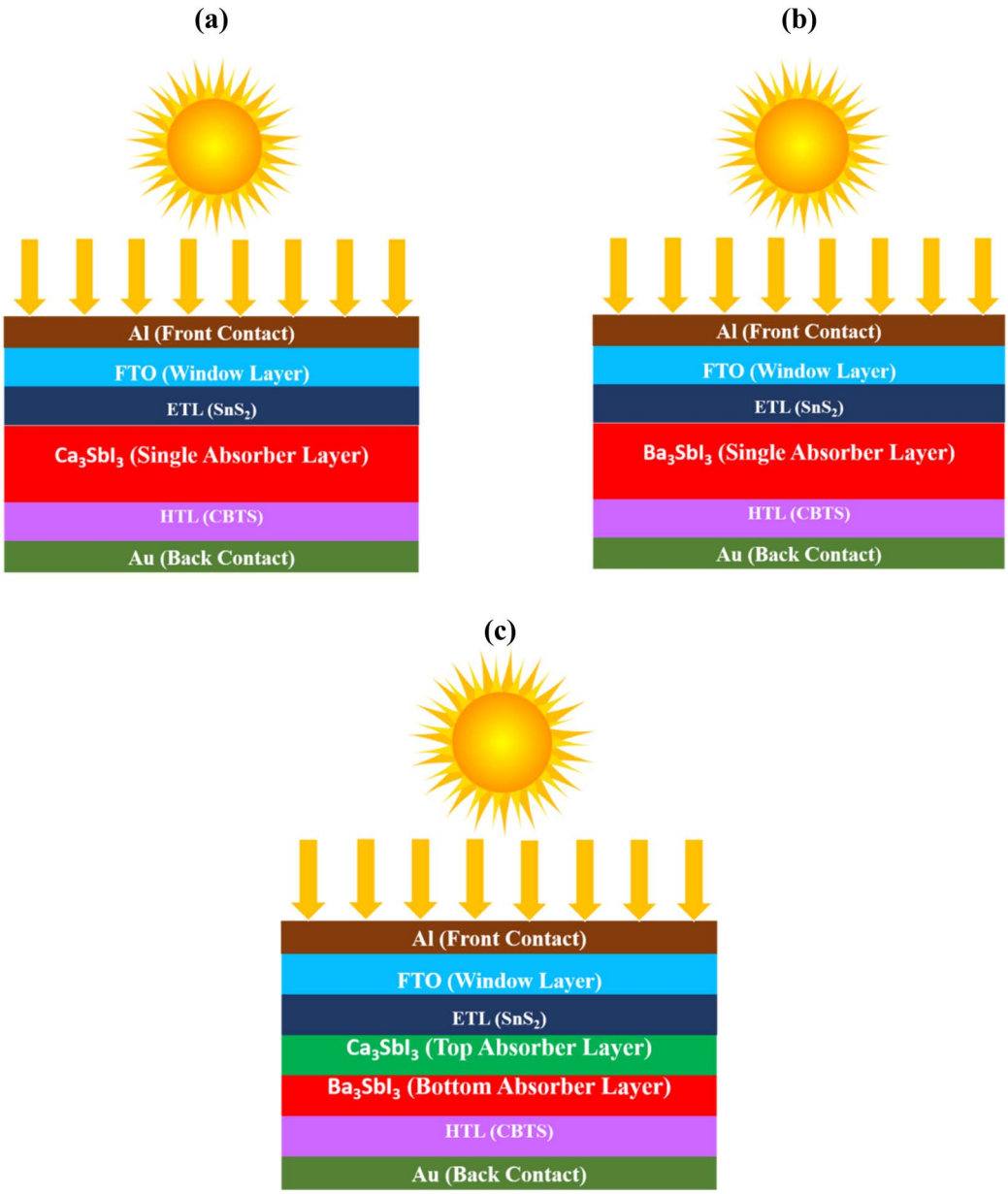

Fig. 1 LFPSC model with different AL (a) Ca_3SbI_3, (b) Ba_3SbI_3, (c) proposed Ca_3SbI_3/Ba_3SbI_3-based DAPSC model.

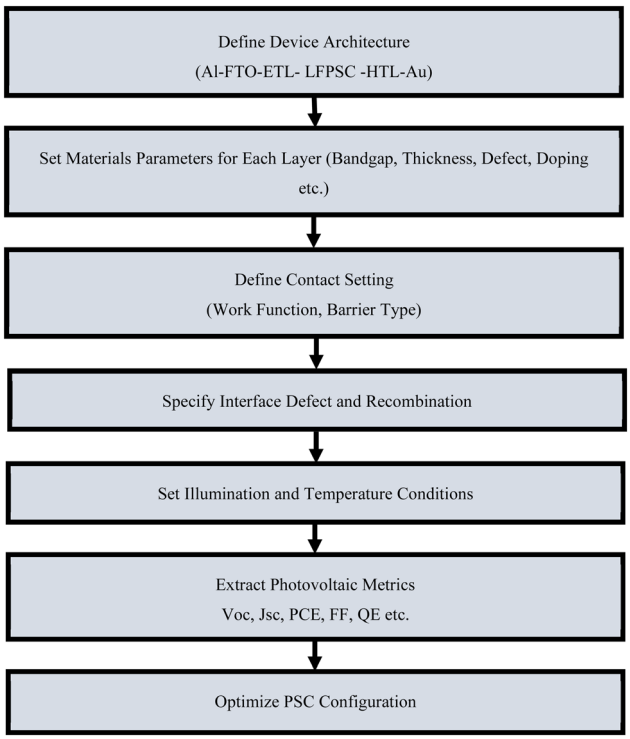

Fig. 2 Simulation process flow employed in SCAPS-1D to extract photovoltaic parameters.

deliver strong performance, while the optimized dual-absorber structure confirms further gains in the key performance metrics. SnS_2 was selected as the ETL due to its ease of fabrication, reduced hysteresis effects.[36–38] CBTS was employed as the HTL for its efficient hole transport, effective charge accumulation, and favorable band alignment that ensure stable and efficient operation.[39] The RFR-based ML model was applied further to the SCAPS-1D simulated data of the proposed DAPSC design to accurately estimate device performance and determine the relative significance of key input parameters. Additionally, Pearson correlation and SHAP values analysis reveal clear linear dependencies between input variables and output responses, highlighting the main factors governing device performance. This combined approach of simulation and ML establishes a novel framework for advancing lead-free DAPSCs, offering an innovative route to expedite the growth of high-performance and environmentally sustainable photovoltaic applications.[40,41]

2. Device structure and methodology

2.1 Inorganic LFPSC model featuring the A_3BX_3 structure

In this work, we conducted SCAPS-1D simulations on a PSC that is entirely inorganic and lead-free, structured according to the A_3BX_3 arrangement. Within this structure, the 'A' site is filled by divalent alkaline earth metal (Ca^{2+}, Ba^{2+}), the 'B' site hosts a trivalent p-block element (Sb^{3+}), and the 'X' site consists of a halide anion (I^-), offering a stable framework for excellent photon absorption and carrier mobility in solar cell applications.[42–44] We explored three different LFPSC configurations to evaluate and optimize device performance, as illustrated in Fig. 1a–c and 2. The first structure, as depicted in Fig. 1a, Al/FTO/SnS_2/Ca_3SbI_3/CBTS/Au, used Ca_3SbI_3 as the

Table 1 Input attributes of FTO, ETL, absorber, and HTL of the LFPSC model[33,53,54]

Parameters	FTO	SnS_2	Ba_3SbI_3	Ca_3SbI_3	CBTS
Thickness (nm)	50	50	1000	300	100
ε_r	10	10	6.02	5.8	5.4
E_g (eV)	3.6	2.24	1.384	1.598	1.9
χ (eV)	4.5	4.24	4.25	4.153	3.6
N_c (cm^{-3})	2.0×10^{18}	2.2×10^{18}	9.613×10^{18}	9.91×10^{18}	2.0×10^{18}
N_v (cm^{-3})	1.8×10^{19}	1.8×10^{19}	1.164×10^{19}	1.74×10^{19}	1.8×10^{19}
μ_e ($cm^2\ V^{-1}\ s^{-1}$)	20	30	50	50	30
μ_h ($cm^2\ V^{-1}\ s^{-1}$)	100	45	50	50	10
N_D (cm^{-3})	1×10^{18}	1×10^{17}	0	0	0
N_t (cm^{-3})	1×10^{14}	1×10^{14}	1×10^{12}	1×10^{12}	1×10^{15}
N_A (cm^{-3})	0	0	1×10^{17}	1×10^{16}	1×10^{18}
Reference	53 and 54	53 and 54	54	33	53

Table 2 Input factors for the interface layers[53]

Input parameters	HTL/absorber	Absorber/ETL
Type of defect	Neutral	Neutral
Cross-sectional area for electron/hole capture (cm^2)	1×10^{-19}	1×10^{-19}
Distribution of energy	Single	Single
Device operating temperature (K)	300	300
E_r (eV)	0.6	0.6
Defect level at interface (cm^{-2})	1×10^{10}	1×10^{10}
Reference	53	53

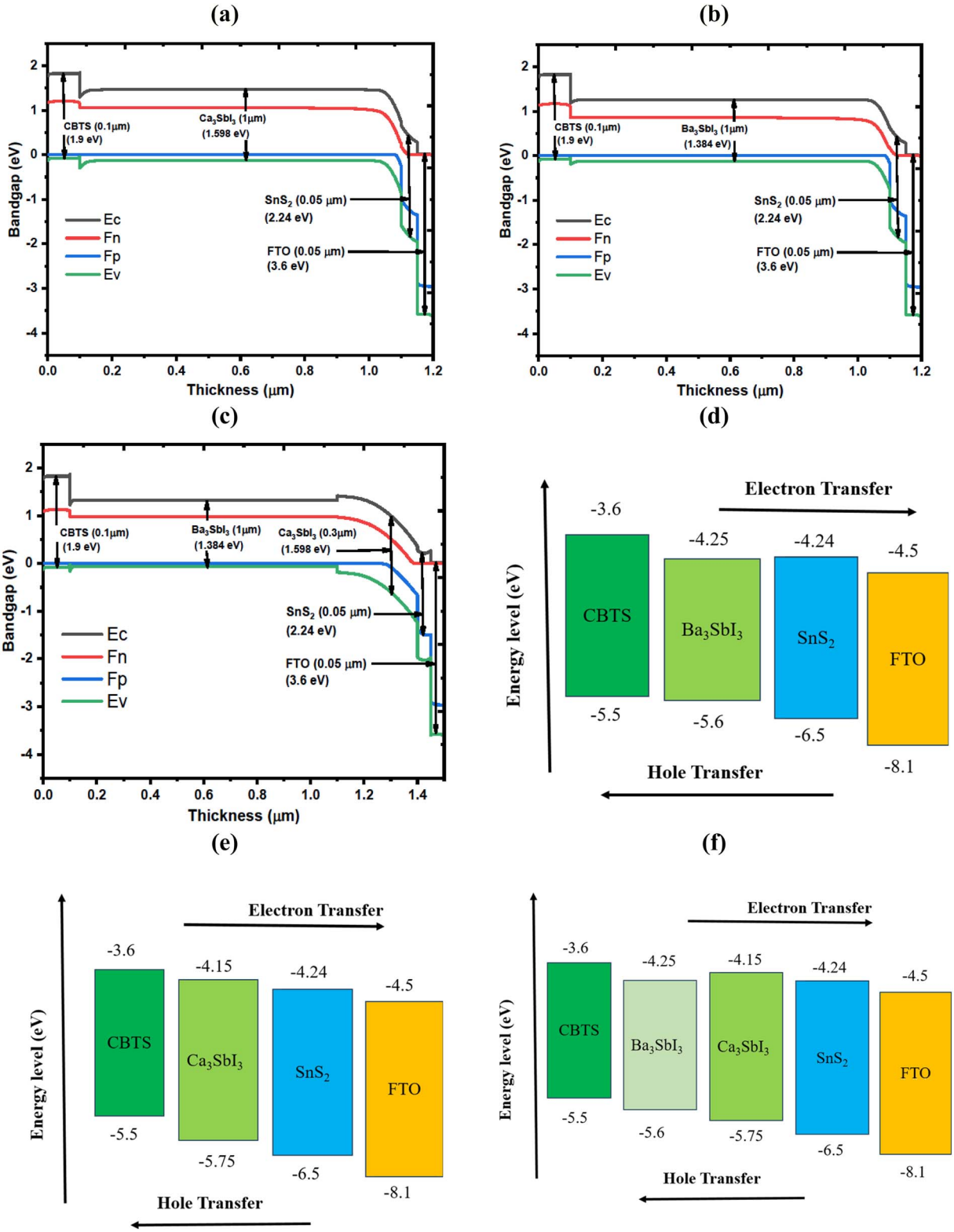

Fig. 3 Energy band diagram of the simulated (a) Ca_3SbI_3 single-absorber, (b) Ba_3SbI_3 single-absorber and (c) dual-absorber Ca_3SbI_3/Ba_3SbI_3-based PSC. Energy band schematics of (d) Ba_3SbI_3, (e) Ca_3SbI_3, and (f) Ca_3SbI_3/Ba_3SbI_3-based PSC.

single absorber layer, with SnS_2 as ETL and CBTS HTL. Fig. 1b shows the model Al/FTO/SnS_2/Ba_3SbI_3/CBTS/Au, which incorporates Ba_3SbI_3 as the absorber while keeping the same ETL and HTL. The proposed novel dual-absorber PSC configuration Al/FTO/SnS_2/Ca_3SbI_3/Ba_3SbI_3/CBTS/Au, as shown in Fig. 1c, combines Ca_3SbI_3 as the top absorber and Ba_3SbI_3 as the bottom absorber, enabling broader spectral absorption, improved charge separation, and enhanced overall efficiency. In our analysis, aluminum (Al) was used for the front electrode (work function: 4.2 eV), FTO was incorporated for the transparent window layer, and gold (Au, work function of 5.4 eV) formed the back electrode.

2.2 Device structures using SCAPS-1D

In this research, SCAPS-1D, developed by Prof. Marc Burgelman, was employed to simulate solar cell devices.[45–47] We have selected this simulation software because of its established accuracy and widespread use in perovskite solar cell research, with consistent results in earlier studies.[48,49] We analyzed the behavior of multilayer LFPSC in SCAPS-1D by solving relevant semiconductor equations, including Poisson's equation, electron and hole continuity equations, and drift-diffusion transport models.[50] By solving equations to define the device structure, SCAPS-1D computes key photovoltaic performance parameters, including short-circuit current, open-circuit voltage, fill factor, and overall conversion efficiency.[51,52] In this study, we examined three different device structures, as shown in Fig. 1a–c, among which the dual-absorber configuration demonstrated outstanding performance. Our proposed dual absorber model consisted of a window layer (FTO), an ETL (SnS_2), two stacked absorbers (Ca_3SbI_3 as the wide energy gap top layer and Ba_3SbI_3 as the narrow energy gap bottom layer), a hole transport layer (CBTS), and a back contact made of gold

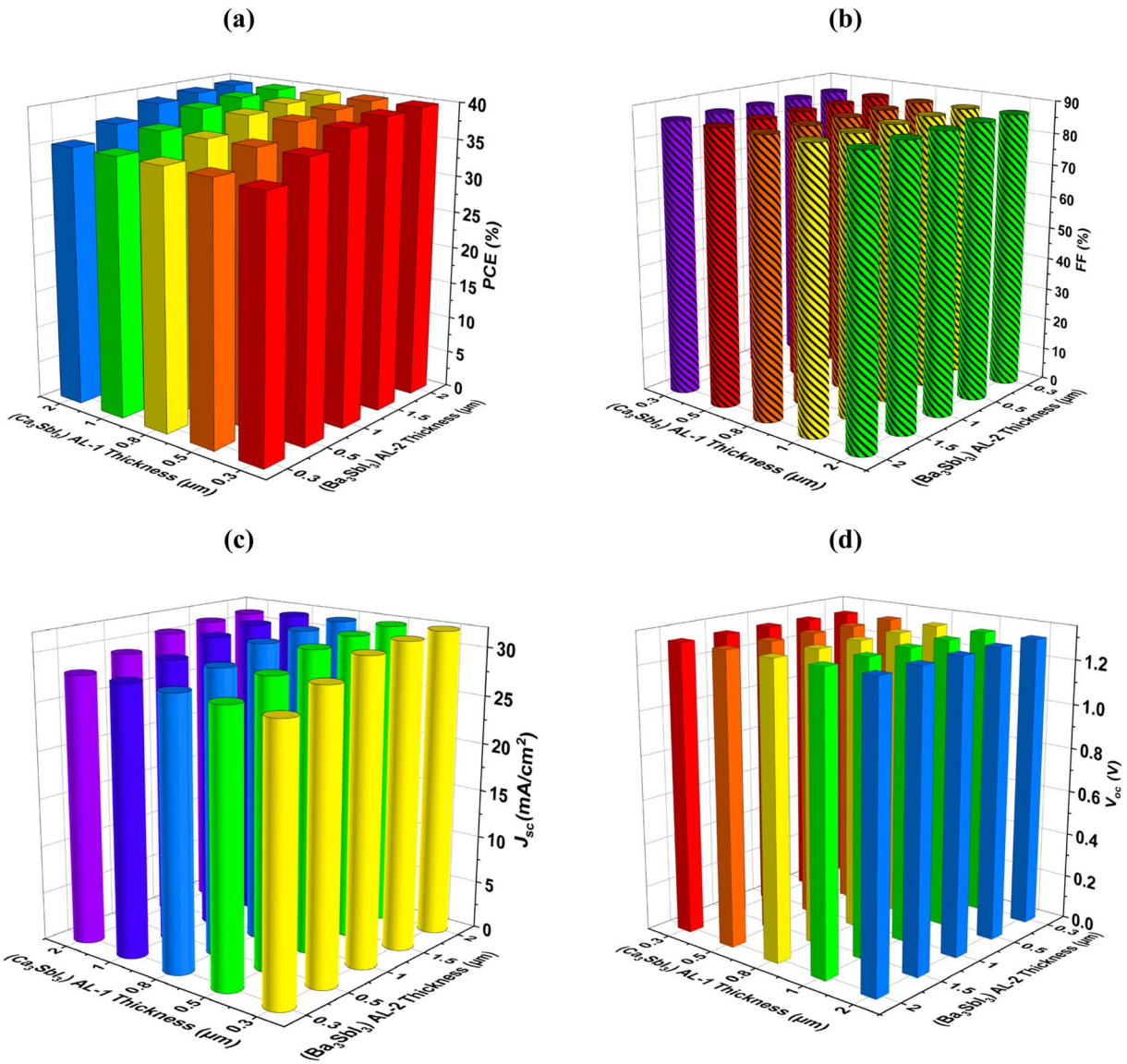

Fig. 4 Impression of AL thickness on (a) PCE, (b) FF, (c) V_{oc} and (d) J_{sc} of the DAPSC model.

(Au). The simulations were executed using conventional test parameters, such as AM1.5G solar spectrum exposure at 300 K temperature and an incoming light intensity of 1000 W m^{-2}.

The simulation of the PSC was executed in SCAPS-1D by first constructing the layered structure: Al/FTO/ETL/LFPSC/HTL/Au. For each layer, key physical properties, such as energy bandgap, thickness, carrier concentration, defect levels, and mobility, were assigned based on literature and preliminary optimization as shown in Tables 1 and 2. The electrical contacts were defined with appropriate work functions and barrier types to realistically model charge injection and collection. Interface layers were carefully modeled to include defect states and recombination processes and to capture losses that occur at layer boundaries. To evaluate the impact of material and device parameters, deliberate variations were implemented to the factors such as dopant concentration, defect densities, structural thicknesses, resistance components, and device operational temperature. The key performance metrics PCE, V_{oc}, J_{sc}, FF, J–V characteristics, and quantum efficiency spectra were examined to assess device achievement and guide the optimization of the dual-absorber PSC configuration.

2.3 Machine learning for predicting DAPSC performance

In this research, an RFR model was employed to forecast PSCs' performance for its capacity to process high-dimensional datasets while minimizing overfitting and preserving interpretability. The ML model was designed and evaluated on the SCAPS-1D generated dataset, including critical performance indicators such as PCE, V_{oc}, J_{sc}, and FF, and implemented through the scikit-learn library in Python.[55] The RFR model was assessed using the determination coefficient (R^2), root mean squared error (RMSE) and Mean Absolute Error (MAE),[56] where R^2 indicates proportion of variance in the data captured by the model, RMSE measures the average size of forecast errors in the same units as the target and MAE exhibits the mean absolute difference between predicted and simulated values. Finally, the influence of each parameter in the photovoltaic behavior of the optimized DAPSC was examined using Pearson correlation and Shapley Additive exPlanations values, enabling identification of

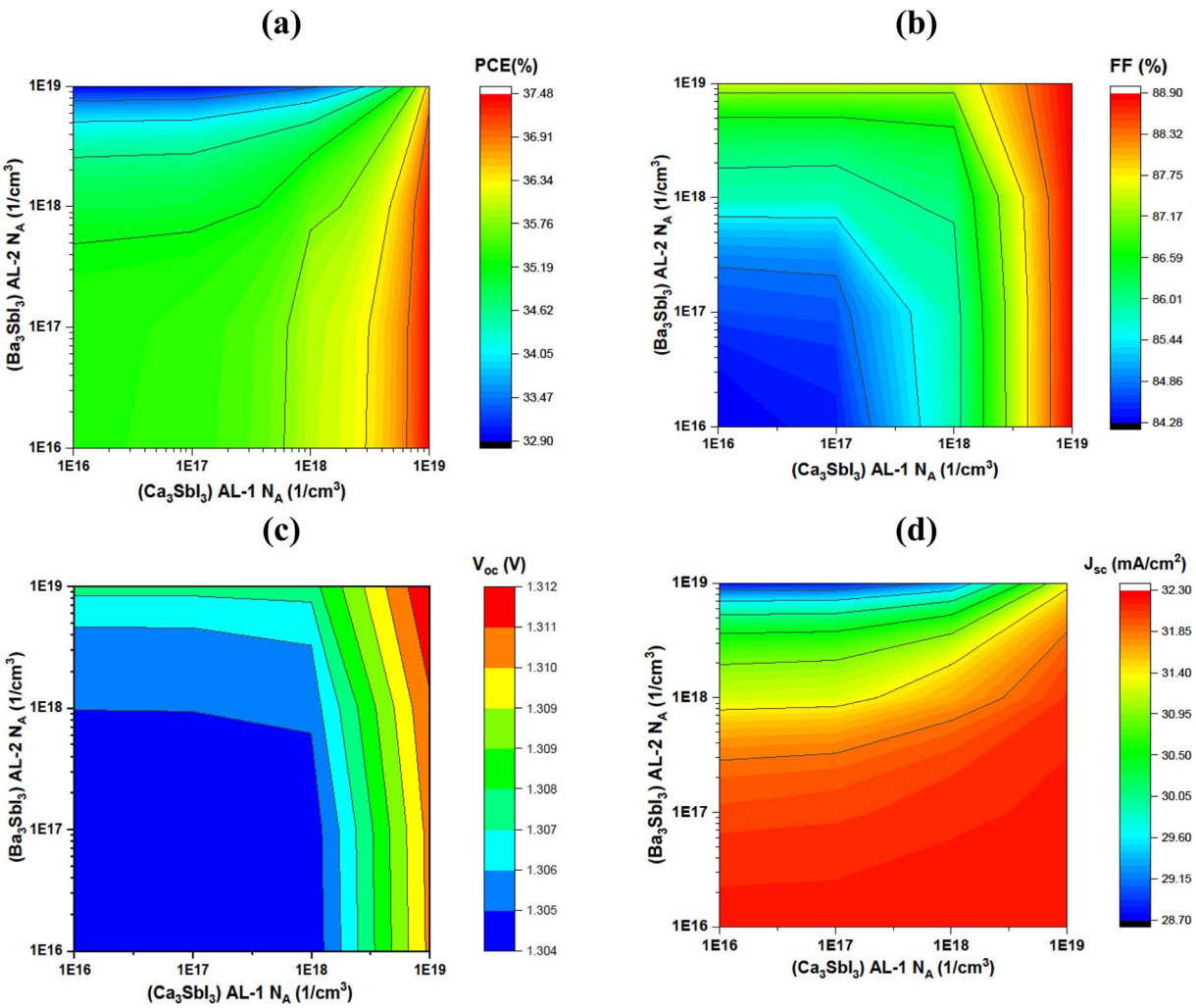

Fig. 5 Impression of top and bottom absorber doping concentration on (a) PCE, (b) FF, (c) V_{oc}, and (d) J_{sc} of the proposed DAPSC model.

the most impactful parameters. Hyperparameter optimization was conducted to improve the model's predictive accuracy by adjusting key parameters, including the number of trees, minimum leaf size, tree depth, bootstrap sampling, feature subsampling, and learning rate, ensuring accurate and reliable performance.[57,58]

3. Results and discussion

3.1 Energy band analysis of LFPSC model

Fig. 3 shows the energy levels, where E_c = conduction band, E_v = valence band, F_n = electron quasi-Fermi level, and F_p = hole quasi-Fermi level. The energy distributions across the different layers of the PSC configuration, as illustrated in Fig. 3a–f, highlight that proper alignment facilitates effective charge transfer and significantly influences the solar cell efficiency.[59,60] Single-absorber PSCs are depicted in Fig. 3a, b and d, e, where Ca_3SbI_3 and Ba_3SbI_3 are used as active light-harvesting layers. The Ca_3SbI_3 with a wide bandgap of 1.598 eV effectively absorbs high-energy photons, while electrons and holes are transported *via* the SnS_2 (ETL) and CBTS (HTL), respectively. Ba_3SbI_3 with a narrower bandgap of 1.384 eV, captures lower-energy photons such as red and near-infrared light. Beyond their complementary bandgaps, Ca_3SbI_3 and Ba_3SbI_3 were chosen due to their common material family, similar electronic properties, and reported stability. Their defect tolerance and well-aligned energy levels facilitate efficient charge transfer and reduced recombination in a dual-absorber configuration. From SCAPS-1D simulation analysis, the Ca_3SbI_3 single-absorber LFPSC delivered a V_{oc} = 1.37 V, PCE = 29.13%, J_{sc} = 24.50 mA cm^{-2}, and FF = 87.01%, whereas the Ba_3SbI_3 single-absorber LFPSC obtained a V_{oc} of 1.21 V, PCE of 33.31%, J_{sc} = 32.17 mA cm^{-2}, and FF = 85.81%. The proposed optimized lead-free dual-absorber PSC configuration (Ca_3SbI_3 as top AL, Ba_3SbI_3 as bottom AL), as demonstrated in Fig. 3c and f, employs a graded bandgap design that allows sequential absorption of high- and low-energy photons.[61] This staggered band alignment enhances charge separation, reduces recombination, and improves current collection. The proposed DAPSC design showed improved results: V_{oc} = 1.30 V, PCE = 36.03%, J_{sc} = 32.18 mA cm^{-2}, and FF = 85.84%. These outcomes promise the benefits of the dual-absorber strategy, showing broader spectrum

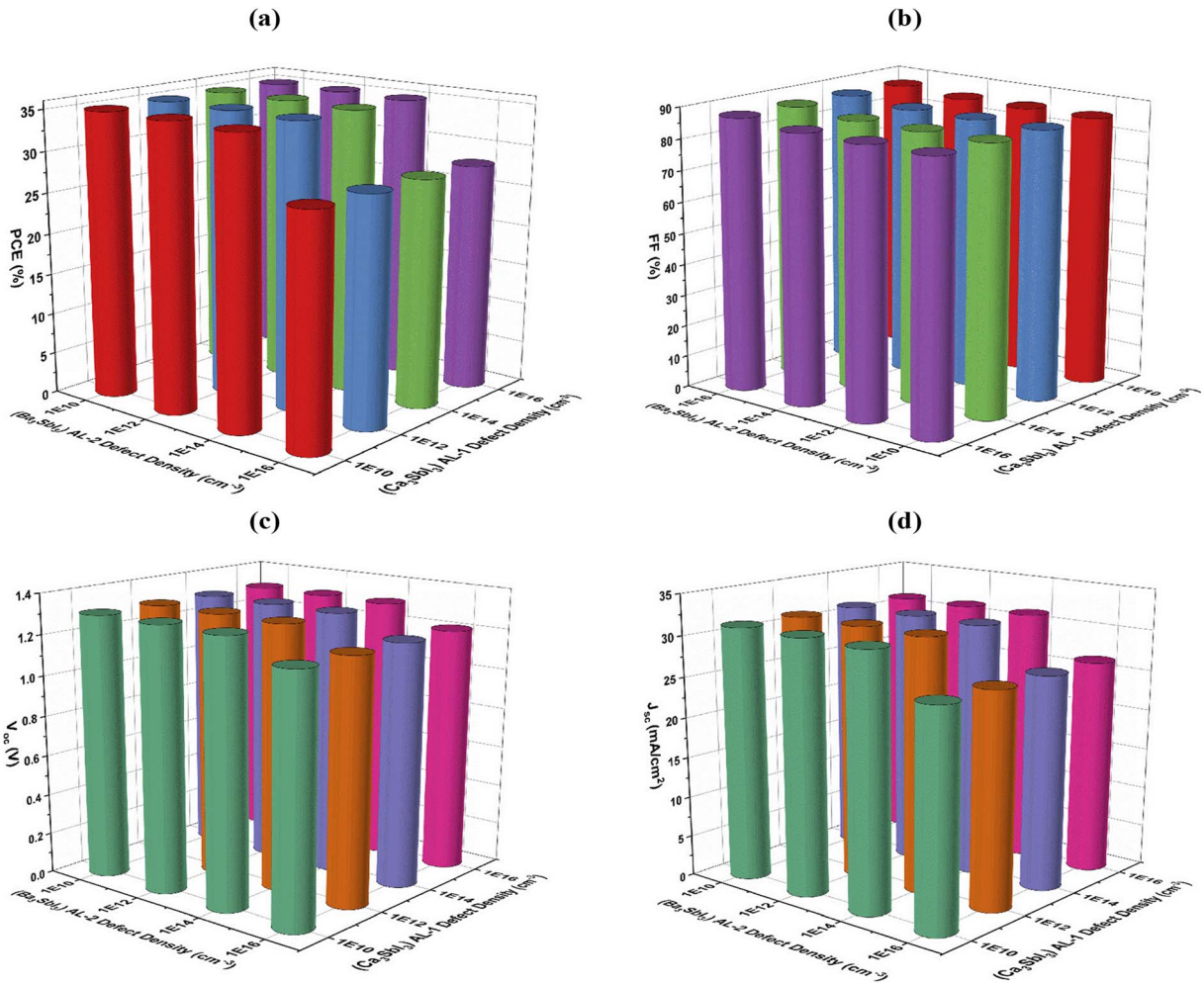

Fig. 6 Impact of AL defect density on device metrics: PCE (a), FF (b), V_{oc} (c) and J_{sc} (d) of the proposed DAPSC model.

utilization, higher efficiency, and enhanced stability compared with single-absorber configurations.[62]

3.2 Effect of AL thickness on the proposed DAPSC

As demonstrated in Fig. 4a–d, varying the AL thicknesses (Ca_3SbI_3 as AL-1 and Ba_3SbI_3 as AL-2) from 0.3 to 2 μm, the device gained optimal performance at AL-1 = 0.30 μm combined with AL-2 = 1.00 μm. The changes shown in Fig. 4 support that AL thickness plays an important role in device performance, stressing the necessity of AL selection in dual-absorber PSC design. The resulting DAPSC structure exhibited PCE = 36.03%, J_{sc} = 32.17 mA cm^{-2}, V_{oc} = 1.304 V, and FF = 85.83%, retaining top AL doping density of 1 × 10^{16} cm^{-3} and bottom AL doping density of 1 × 10^{18} cm^{-3}. So, the performance of dual-absorber PSC is highly influenced by AL thickness. A thicker top absorber boosts light absorption by allowing more high-energy photons to be captured and thereby enhancing the J_{sc}. Similarly, optimization of the bottom absorber thickness ensures effective absorption of lower-energy photons transmitted through the top layer, improving the overall PCE. However, an overly thick layer can contribute to higher series resistance and reduced charge collection efficiency, which may slightly suppress FF (%) and V_{oc} (V). So, an optimal balance between the two absorber layers is essential to balance light harvesting and charge transport, achieving improved device efficiency.[63] From this point onward, all subsequent analyses of the proposed DAPSC structure were carried out by implementing absorber thicknesses of 0.30 μm for Ca_3SbI_3 (top layer) and 1.00 μm for Ba_3SbI_3 (bottom layer). These results highlight the key impact of careful adjustment of AL thickness in achieving reliable, improved performance of dual-absorber PSCs.[64]

3.3 Impact of AL doping density on the proposed DAPSC model

The influence of AL doping was examined by varying Ca_3SbI_3 (top AL) and Ba_3SbI_3 (bottom AL) concentrations from 1 × 10^{16} to 1 × 10^{19} cm^{-3}. The outcomes presented in Fig. 5a–d shows

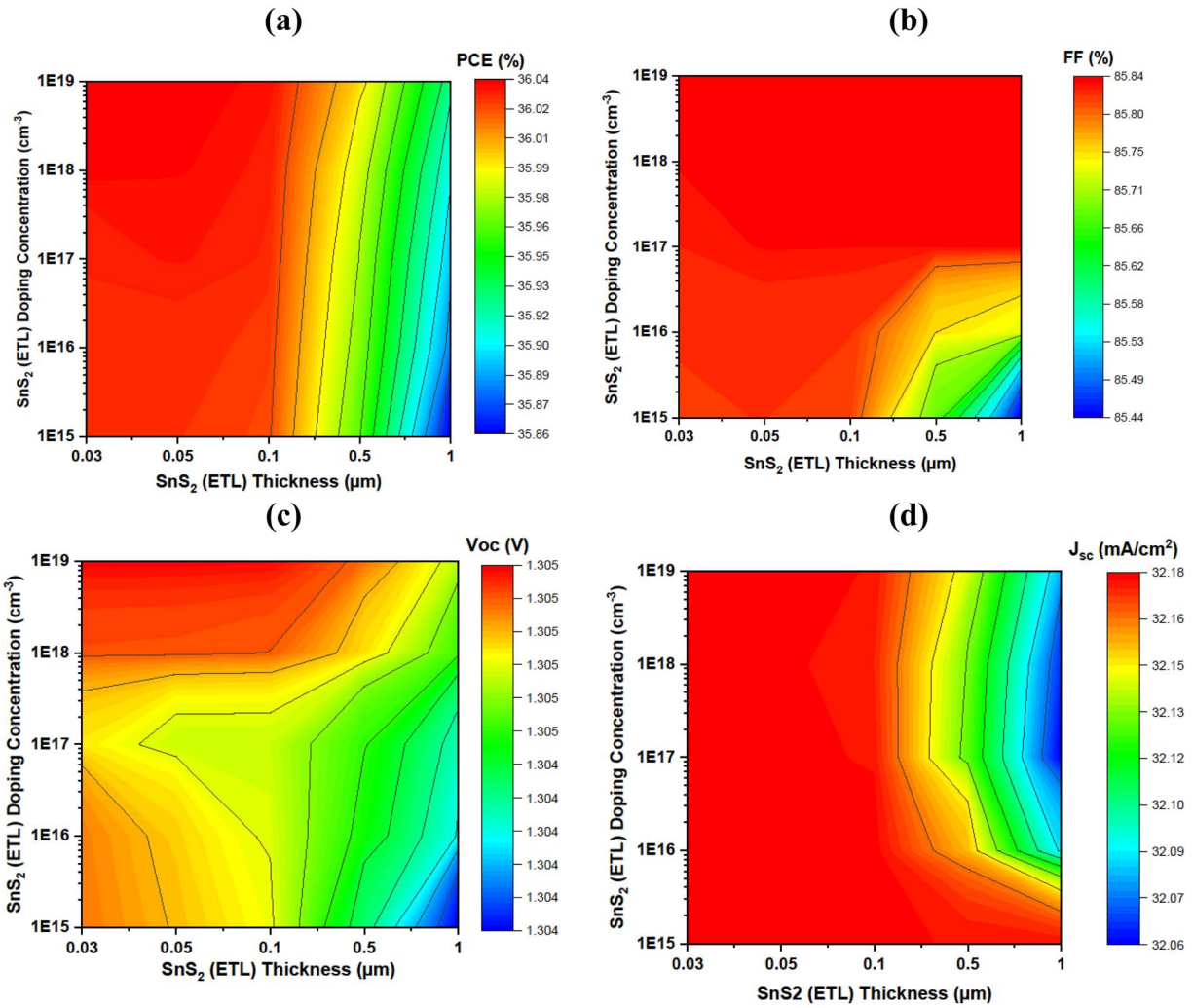

Fig. 7 Impact of ETL on PCE (a), FF (b), V_{oc} (c) and J_{sc} (d) of the proposed DAPSC model.

that, at lower doping ($1 \times 10^{16}/1 \times 10^{16}$ cm^{-3}), the cell reached a PCE = 35.37%, J_{sc} = 32.17 mA cm^{-2}, V_{oc} = 1.304 V and FF = 84.28%. Increasing top AL doping to 1×10^{18} cm^{-3} when bottom AL is set at 1×10^{16} cm^{-3}, we found slightly reduced J_{sc} (31.21 mA cm^{-2}) but improved FF (85.87%), yielding a still-high PCE of 34.98%. We noticed at high doping level ($1 \times 10^{19}/1 \times 10^{16}$ cm^{-3}), V_{oc} peaked to 1.307 V and FF to 87.49%, but J_{sc} dropped sharply to 28.78 mA cm^{-2}, reducing efficiency to 32.92%. When the bottom layer doping increased, performance improved further. At $1 \times 10^{16}/1 \times 10^{18}$ cm^{-3}, the cell delivered 36.03% PCE, J_{sc} = 32.17 mA cm^{-2}, V_{oc} = 1.305 V and FF = 85.83%. The highest efficiency of 37.48% was recorded at $1 \times 10^{16}/1 \times 10^{19}$ cm^{-3}, with J_{sc} = 32.17 mA cm^{-2}, V_{oc} = 1.310 V and FF = 88.89%. However, heavy doping is less practical due to increased recombination and instability. So, while very high doping yields record efficiency, the optimum balance occurs at Ca_3SbI_3 (1×10^{16} cm^{-3})/Ba_3SbI_3 (1×10^{18} cm^{-3}), where the device achieves PCE = 36.03%, J_{sc} = 32.17 mA cm^{-2}, V_{oc} = 1.305 V, and FF = 85.83%, ensuring both high efficiency and stability.

3.4 AL defect density impact

The role of absorber layer defect level in device properties was explored by varying defect concentrations in both the Ba_3SbI_3 absorber as well as the Ca_3SbI_3 absorber, as presented in Fig. 6a–d. The device metrics stayed largely unchanged for defect levels between 1×10^{10} cm^{-3} and 1×10^{14} cm^{-3}, with stable outputs of approximately V_{oc} = 1.31 V, J_{sc} = 31.2 mA cm^{-2}, FF = 85–86%, and PCE = 35%. However, when the Ba_3SbI_3 bottom layer defect density increased to 1×10^{16} cm^{-3}, performance deteriorated sharply, with PCE reduced to around 28% and corresponding decreases in V_{oc} and J_{sc}. This loss is linked to enhanced carrier recombination and reduced lifetime. In contrast, higher defect densities in the top layer produced minimal influence, validating that device efficiency is predominantly governed by defect states in the bottom AL.

3.5 Effect of SnS_2 as ETL

The influence of SnS_2 (ETL) thickness and donor density on device outputs was evaluated as outlined in Fig. 7a–d and 8. The

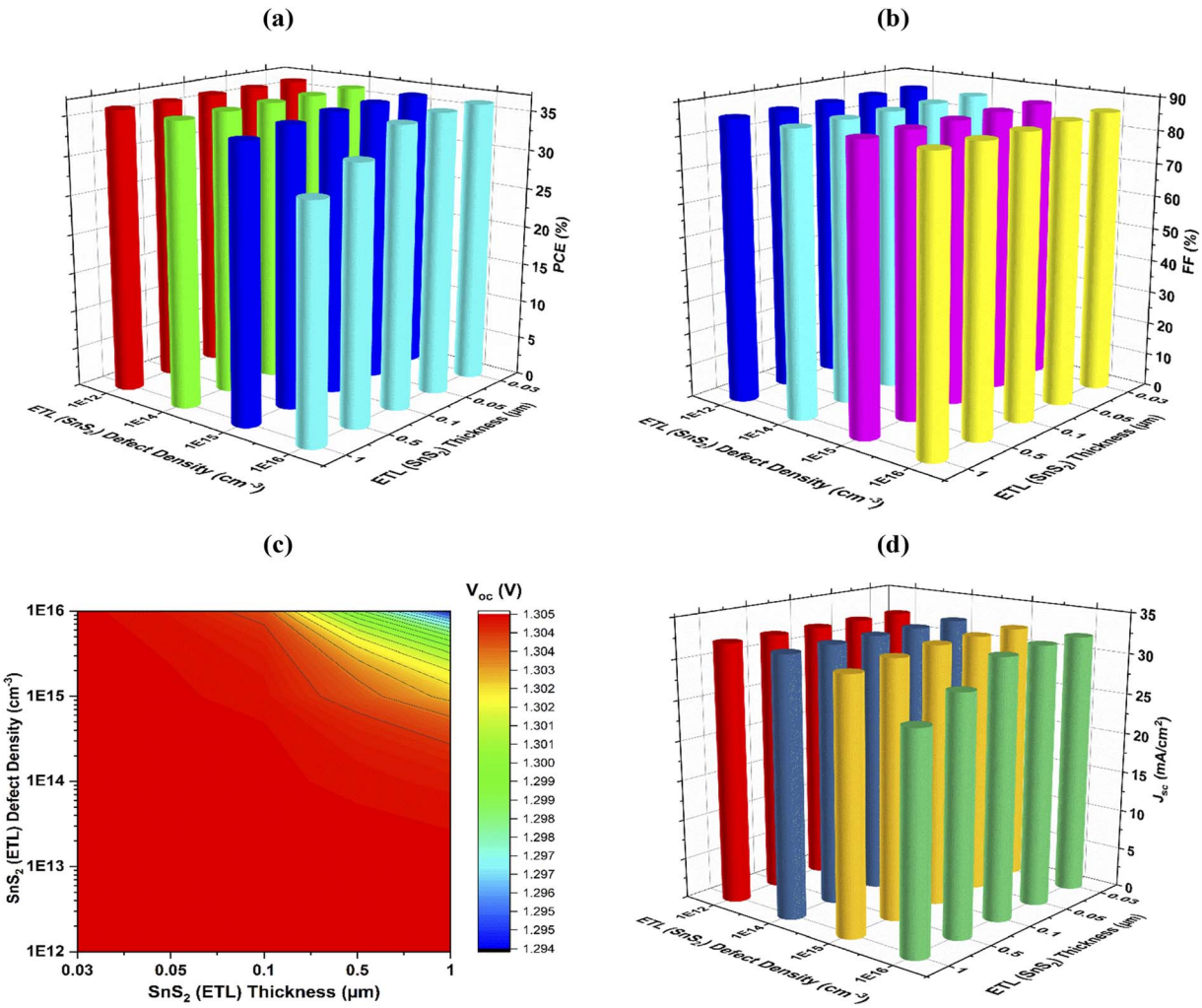

Fig. 8 Effect of ETL thickness and defect density on (a) PCE, (b) FF, (c) V_{oc} and (d) J_{sc} of the proposed DAPSC model.

results depict that ETL thickness is the dominant factor, while donor density has only a marginal effect. For thin ETL (0.03–0.10 μm), the device maintained a high efficiency (36.03%) with stable values of V_{oc} (1.30 V), J_{sc} (32.18 mA cm^{-2}), and FF (85.84%). Increasing the thickness to 0.50 μm led to a slight drop in efficiency caused mainly by reduced J_{sc}, while V_{oc} remained unchanged. By altering the donor level from 1×10^{16} cm^{-3} to 1×10^{19} cm^{-3}, we observed negligible changes in all photovoltaic parameters. The V_{oc} remained constant, and only small fluctuations in J_{sc} and FF were noted.

Furthermore, the performance of the device was investigated by changing the SnS_2 (ETL) thickness along with its defect level. We found that defect density has little effect on thin ETL but strongly impacts thicker layers. For very thin ETLs (0.03–0.05 μm), PCE (~36%), J_{sc} (~32.18 mA cm^{-2}), V_{oc} (1.30 V), and FF (~85.8%) remain stable across defect densities up to 1×10^{16} cm^{-3}, indicating good tolerance to imperfections. At 0.10 μm thickness, a slight efficiency drop appears with higher defects, while at 0.50–1.00 μm the effect is severe. These findings indicate that ETL thickness primarily controls charge transport and device performance, whereas donor density has a minimal impact. Therefore, we observed in this study that the device achieved optimized performance at ETL thickness of 0.05 μm, doping level of 1×10^{17} cm^{-3}, and defect level of 1×10^{14} cm^{-3}, reaching a PCE of 36.03% with V_{oc} = 1.30 V, J_{sc} = 32.18 mA cm^{-2}, and FF = 85.84%.

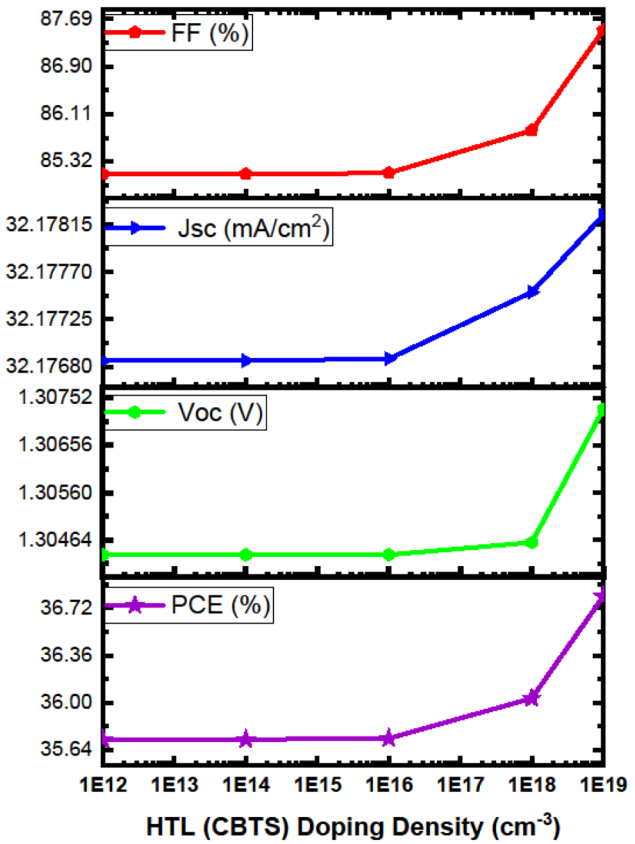

Fig. 9 HTL doping effect on the proposed lead-free DAPSC model.

3.6 Influence of CBTS as HTL

In our analysis, we carefully investigated how HTL acceptor concentration influences the introduced lead-free dual-absorber PSC model performance. We noticed in Fig. 9 that PCE was affected by acceptor levels, increasing from approximately 35.7% at 1×10^{12} to 1×10^{16} cm^{-3} to 36.81% at 1×10^{19} cm^{-3}, and a rise in FF ranging from 85.1% to 87.50%. We also observed that the highest performance was consistently obtained at a dopant density of 1×10^{19} cm^{-3}, demonstrating the dominance of acceptor density in enhancing device performance.

The impression of CBTS defect levels on device results was explored for HTL thicknesses from 0.03 to 1.00 μm. From Fig. 10a–d, across all thicknesses and defect densities (1×10^{12} to 1×10^{16} cm^{-3}), the PCE remained constant at 36.03%, J_{sc} = 32.18 mA cm^{-2}, V_{oc} = 1.30 V, and FF = 85.83–85.84%. The analysis indicates that device performance is largely unaffected by CBTS defect density within this range, reflecting device stability and resistance to moderate defect densities.

3.7 Interface layer defect density analysis

Fig. 11 shows the consequences of interface defects in determining the performance of three heterojunction configurations: CBTS/Ba_3SbI_3, Ba_3SbI_3/Ca_3SbI_3, and Ca_3SbI_3/SnS_2. At a lower defect density of 1×10^{10} cm^{-3}, our proposed lead-free DAPSC model exhibits high performance with a PCE of 36.03%, V_{oc} of 1.30 V, J_{sc} of 32.18 mA cm^{-2}, and FF of 85.84%, indicating minimal influence of defects at this level. Performance declines as defect density rises, and CBTS/Ba_3SbI_3 shows the steepest drop to 16.25% PCE at 1×10^{18} cm^{-3}, while Ba_3SbI_3/Ca_3SbI_3 reduces to 14.63%. We observed that Ba_3SbI_3/SnS_2, however, maintains a higher PCE of 23.71% and J_{sc} above 31 mA cm^{-2} at the same defect density, demonstrating its superior tolerance to interfacial defects. These trends show that interface quality strongly affects carrier extraction, and choosing defect-resilient interfaces is crucial for stable device operation.[65]

3.8 Temperature response

The temperature-dependent performance of three PSC configurations, single-absorber Al/FTO/SnS_2/Ba_3SbI_3/CBTS/Au, single-absorber Al/FTO/SnS_2/Ca_3SbI_3/CBTS/Au, and the proposed lead-free dual-absorber PSC model Al/FTO/SnS_2/Ca_3SbI_3/Ba_3SbI_3/CBTS/Au—was explored through 300–500 K as illustrated in Fig. 12. The proposed dual-absorber PSC presents higher initial performance, achieving a PCE = 36.03% at 300 K, with J_{sc} = 32.18 mA cm^{-2}, V_{oc} = 1.30 V, and FF = 85.84%. As the temperature rises to 500 K, PCE gradually decreases to 30.09%, FF to 82.30%, and V_{oc} to 1.14 V, while J_{sc} remains steady. In comparison, the single-absorber Ca_3SbI_3 device shows a lower initial PCE (29.13%) and declines more steeply to 22.54% at 500 K, whereas the Ba_3SbI_3 single-absorber PSC starts at 33.31% and reduces to 24.71%. The proposed all-inorganic PSC (Al/FTO/SnS_2/Ca_3SbI_3/Ba_3SbI_3/CBTS/Au) integrates stable ETL and HTL that further mitigate typical degradation mechanisms. The temperature-dependent simulations manifest electrical

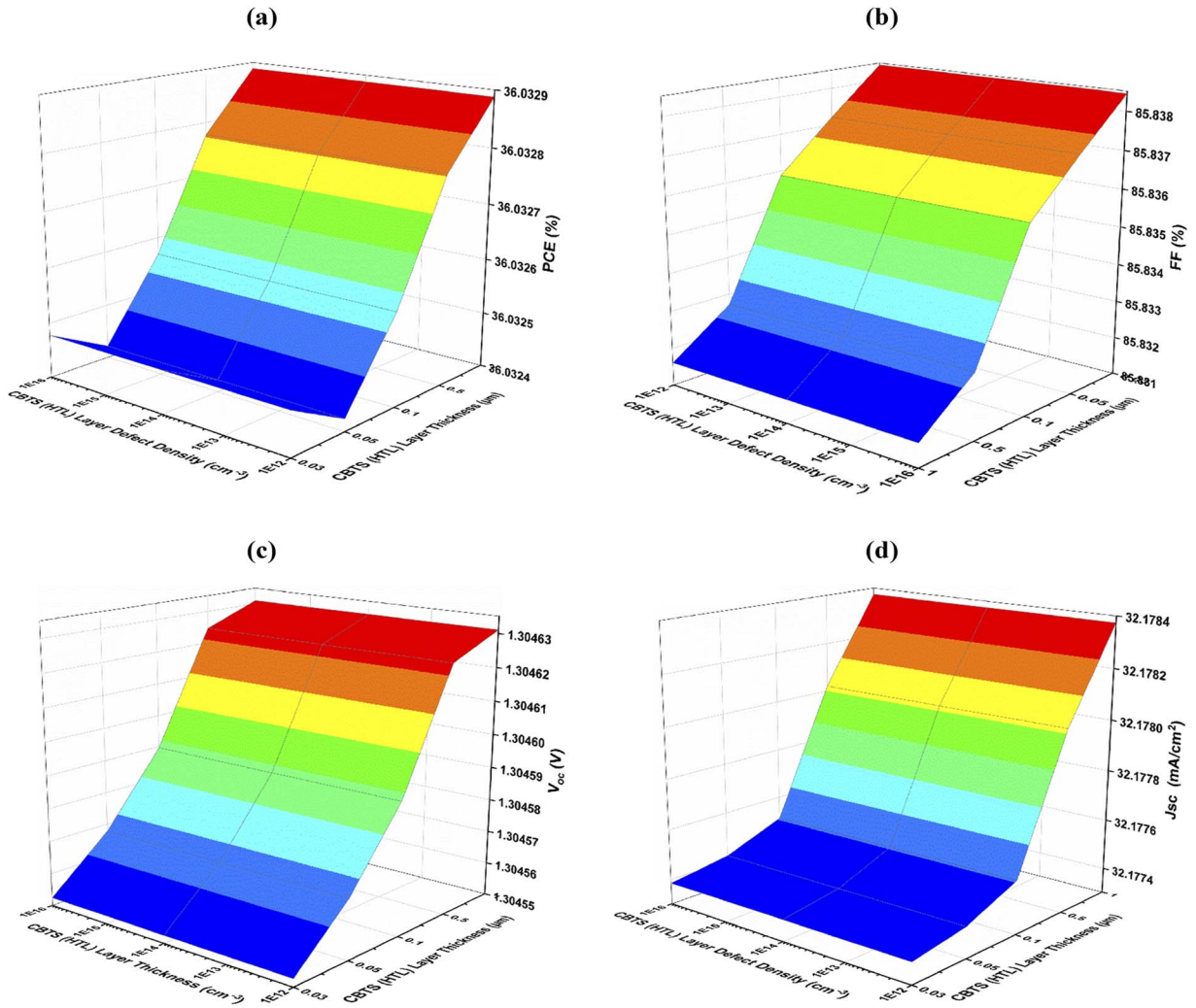

Fig. 10 Effect of (CBTS) HTL thickness as well as defect on (a) PCE, (b) FF, (c) V_{oc} and (d) J_{sc} of the proposed lead-free DAPSC model.

performance trends and do not directly capture chemical or structural degradation such as phase transitions, ion migration, or decomposition. Although experimental validation is required, the presented dual-absorber configuration is anticipated to ensure superior thermal, moisture, oxygen, and illumination stability compared to conventional LFPSCs. These results imply that the proposed configuration effectively combines the complementary advantages of Ca_3SbI_3 and Ba_3SbI_3 absorbers, providing both higher efficiency and enhanced thermal stability. The performance trends emphasize its promise as a robust, improved-efficiency, lead-free PSC design suitable for practical applications under varying environmental and temperature conditions.

3.9 Series & shunt resistance analysis

We analyzed the impact of series resistance (R_s) on three lead-free PSC architectures as shown in Fig. 13a: Al/FTO/SnS_2/Ca_3SbI_3/CBTS/Au, Al/FTO/SnS_2/Ba_3SbI_3/CBTS/Au, and dual-absorber Al/FTO/SnS_2/Ca_3SbI_3/Ba_3SbI_3/CBTS/Au. Increasing R_s up to 10 Ω cm^2 led to reduced PCE and FF, when V_{oc}, along with J_{sc}, remained almost steady, confirming that resistive losses mainly degrade the fill factor. Among the devices, the dual-absorber cell retained the highest efficiency, falling from 36.03% to 26.46%, whereas Ca_3SbI_3 and Ba_3SbI_3 dropped to 23.52% and 23.74%, respectively. These results show that the dual-absorber structure offers better tolerance to resistive losses.

We also investigated how R_{sh} affects leakage and recombination, as shown in Fig. 13b. Low R_{sh} caused severe efficiency loss, with Ca_3SbI_3 collapsing to PCE = 1.38% at 10 Ω cm^2. Performance improved as R_{sh} increased, stabilizing near PCE = 29% above 10^3 Ω cm^2. Ba_3SbI_3 showed a similar trend, reaching PCE = 33.31% when $R_{sh} \geq 10^4$ Ω cm^2. The dual-absorber device proved most resilient, sustaining PCE = 23.2% at R_{sh} = 100 Ω cm^2 and recovering to PCE = 36.03% at higher R_{sh} values. Beyond 1×10^5 Ω cm^2, it stabilized with V_{oc} = 1.305 V, J_{sc} =

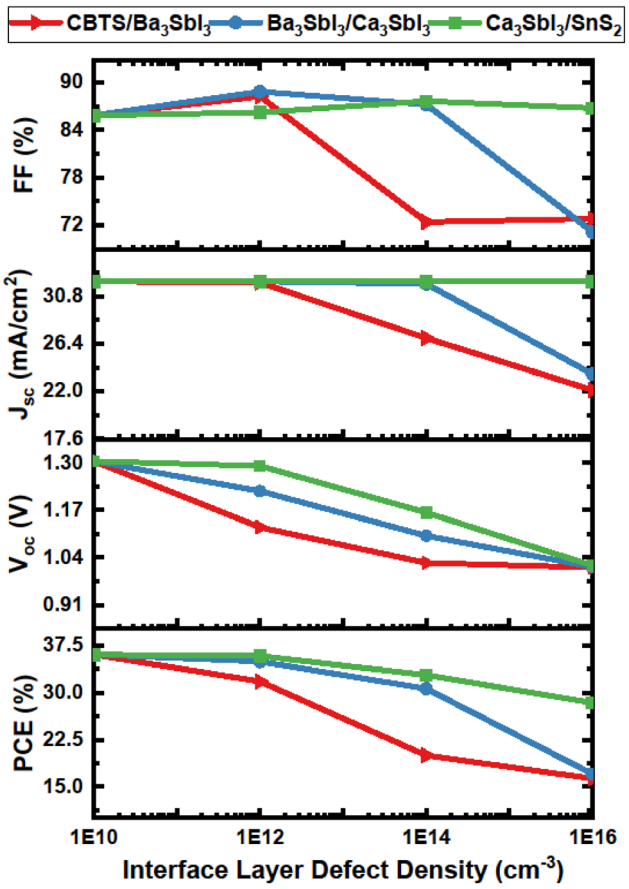

Fig. 11 Device stability analysis under different interface defect densities of the proposed lead-free DAPSC configuration.

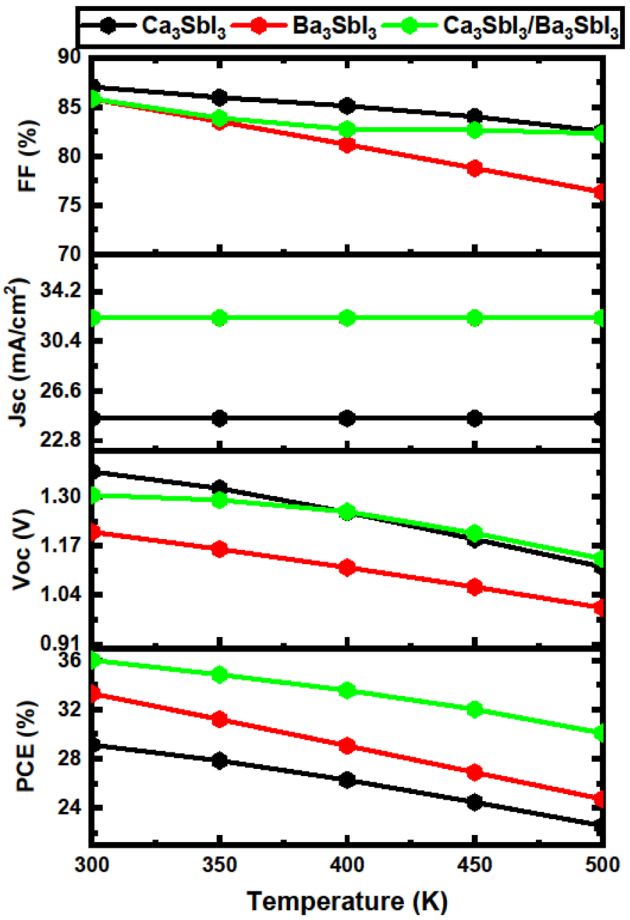

Fig. 12 Device working temperature effect on the proposed PSC model.

32.18 mA cm^{-2}, and FF = 85.84%. The results suggest that the proposed dual-absorber PSC is more stable under shunt variation with enhanced resilience to resistive losses, proving it a reliable lead-free design for practical applications.[65,66]

3.10 *Q–E* and *J–V* analysis

The QE trends as represented in Fig. 14a demonstrate the improved performance of the dual-absorber PSC. The single absorber Ca_3SbI_3-based PSC delivers strong QE within the visible region; however, its response drops sharply beyond 650 nm due to its wider bandgap. In contrast, the Ba_3SbI_3-based PSC exhibits better QE response up to 900 nm, which captures lower-energy photons more effectively. The Ca_3SbI_3/Ba_3SbI_3-based PSC device exhibits a complementary QE response, maintaining greater QE within the visible spectrum and extending infrared absorption up to 900 nm. This broadened QE response resulting from complementary bandgap alignment elevates photon harvesting and carrier generation, thereby clarifying the higher J_{sc} (mA cm^{-2}) of the dual-absorber PSC.[67]

The *J–V* behavior in Fig. 14b validates the enhanced results of the proposed optimized lead-free DAPSC device. The proposed optimized model gains the highest J_{sc} (32.18 mA cm^{-2}), consistent with its extended QE response, while maintaining V_{oc} = 1.305 V, higher than Ba_3SbI_3. The fill factor (FF) is also maximized, indicated by the most rectangular *J–V* curve, reflecting reduced recombination and improved charge transport. Consequently, the dual-absorber PSC achieves the largest area under the *J–V* curve, corresponding to the highest power conversion efficiency (PCE).

3.11 Performance evaluation with reported studies

The performance of the proposed optimized lead-free Ca_3SbI_3/Ba_3SbI_3-based dual-absorber PSC was examined by comparing it with various previously reported devices, as shown in Table 3. While the single-absorber Ca_3SbI_3 and Ba_3SbI_3-based PSC model in this work achieved efficiencies of 29.13% and 33.31%, respectively, the dual-absorber PSC structure Al/FTO/SnS_2/Ca_3SbI_3/Ba_3SbI_3/CBTS/Au delivered an impressive efficiency of 36.03%, supported by a high J_{sc} of 32.18 mA cm^{-2}, V_{oc} of 1.305 V, and FF of 85.84%. This clearly reflects the strength of the optimized lead-free DAPSC design, which ensures superior charge generation, balanced transport, and excellent device

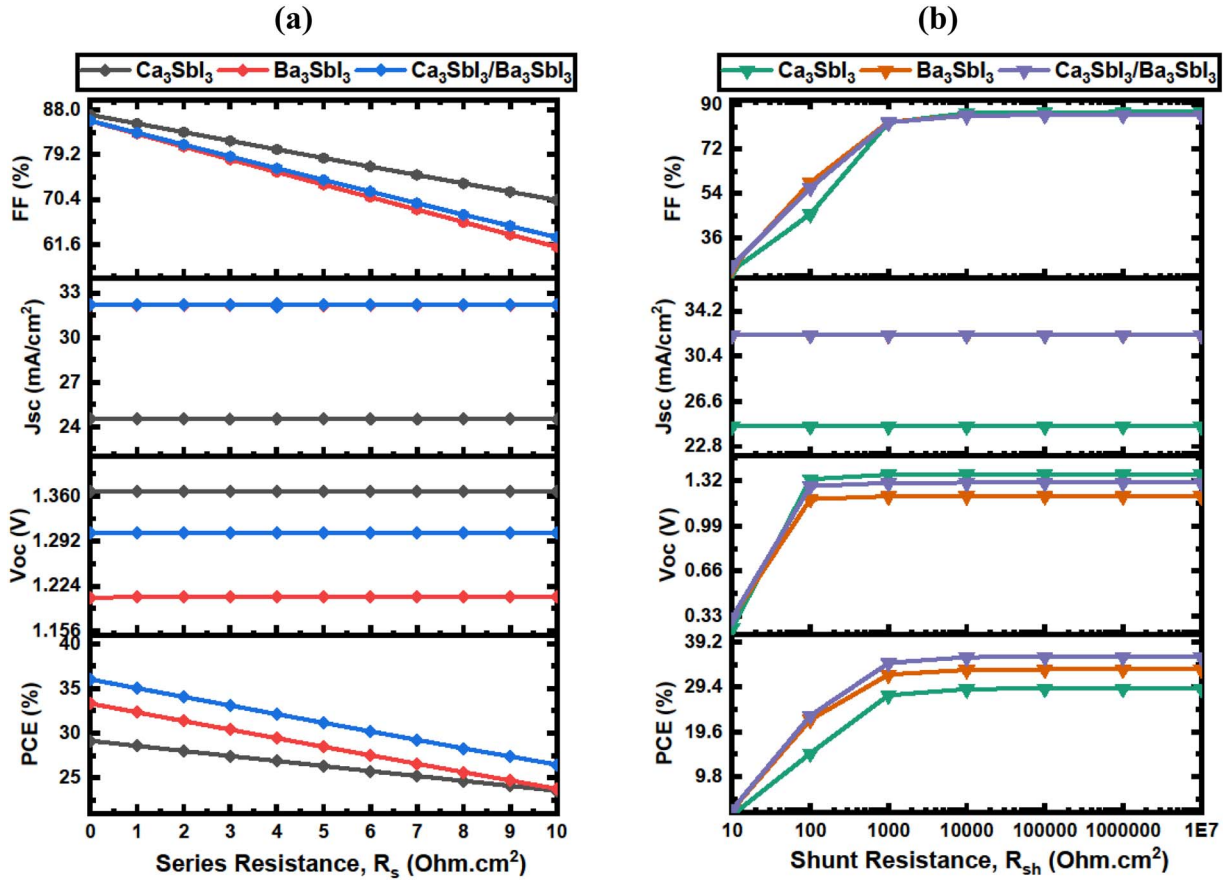

Fig. 13 (a) Series and (b) shunt resistance impact on PSC model.

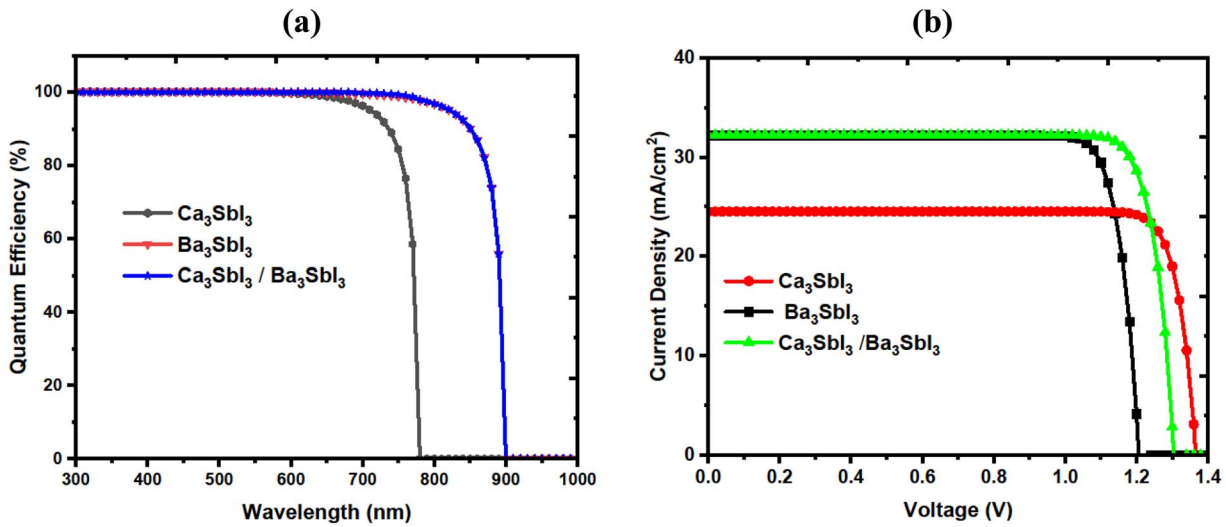

Fig. 14 (a) Optical response evaluation (b) *J*–*V* characterization of the proposed design.

stability for advanced photovoltaic device applications.[76] To the best of our knowledge, experimentally demonstrated $CsSnI_3$-based LFPSC currently obtains efficiency around 12.96% as shown in Table 3, while the proposed Ca_3SbI_3/Ba_3SbI_3-based PSCs have not yet been realized experimentally. So, the performance of the proposed DAPSC is therefore regarded as a theoretical upper bound obtained under idealized simulation

Table 3 Comparative assessment of our proposed PSC and earlier studied devices

Device configuration	PCE (%)	J_{sc} (mA cm^{-2})	FF (%)	V_{oc} (V)	Ref.
$CsPbI_3$/$FAPbI_3$ (experimental)	15.60	17.26	74.00	1.22	68
CdTe/$FeSi_2$ (experimental)	27.35	49.78	83.68	0.6566	69
c-TiO_2/$CsSnI_3$/Spiro-OMeTAD/Au (experimental)	12.96	23.20	65.00	0.86	70
FTO/ZnS/$CsPl_3$/Sr_3PBr_3/Au (simulation)	23.86	25.01	88.38	1.06	71
Ag/FTO/CdS/(Ca_3AsI_3/Ca_3PI_3)/V_2O_5/Ni (simulation)	29.16	25.613	85.33	1.334	72
FTO/SnS_2/Ca_3SbI_3/Sr_3SbI_3/Spiro-OMeTAD/Au (simulation)	32.74	34.17	83.77	1.14	73
Cs_2TiBr_6/La_2NiMnO_6 (simulation)	33.71	43.83	83.85	0.9171	74
$CH_3NH_3PbI_3$/$CsPbI_3$(Simulation)	33.54	27.45	90.49	1.34	75
Al/FTO/SnS_2/Ca_3SbI_3/CBTS/Au	**29.13**	**24.50**	**87.01**	**1.37**	**This work**
Al/FTO/SnS_2/Ba_3SbI_3/CBTS/Au	**33.31**	**32.17**	**85.81**	**1.2068**	**This work**
Al/FTO/SnS_2/Ca_3SbI_3/Ba_3SbI_3/CBTS/Au	**36.03**	**32.18**	**85.84**	**1.305**	**This work**

Table 4 Predictive performance analysis of the proposed DAPSC structure

Performance metrics	R^2 score	MAE score	RMSE score
PCE (%)	0.9586	0.7495	0.9476
FF (%)	0.9747	0.5550	0.7698
J_{sc} (mA cm^{-2})	0.9326	0.4900	0.7736
V_{oc} (V)	0.9879	0.0078	0.0100

conditions and used as a reference point for future experimental exploration.

3.12 Machine learning approach to predict DAPSC performance

RFR-based ML framework was utilized in this research to estimate the performance of the proposed optimized lead-free Ca_3SbI_3/Ba_3SbI_3-based DAPSC model, assess its predictive accuracy, and explore the influence of key input parameters on the proposed device response.[77,78]

3.12.1 Model validation and prediction. To examine the prediction accuracy of the model, we used key statistical indicators- the coefficient of determination (R^2), root mean square error (RMSE) and mean absolute error (MAE).[79,80] These evaluation metrics were applied to the performance parameters, PCE, V_{oc}, J_{sc}, and FF, using a SCAPS-1D simulated dataset. The dataset simulated from the Ca_3SbI_3/Ba_3SbI_3-based PSC model comprises 768 samples; 80% of these were used for model training, and the remaining 20% were used for testing purposes. In the RFR model, the randomized search strategy was employed for hyperparameter optimization, including the number of estimators (100–200), the minimum samples per split (2–7), maximum tree depth (5–10), minimum samples per leaf (1–4), and also maximum features ('sqrt' or 'log2'). The final configuration, number of estimators = 200, maximum depth = 10, minimum samples per split = 2, minimum samples per leaf = 1, maximum features = 'sqrt', was adopted to balance model complexity and generalization, offering flexibility for precise forecasting while controlling over-adaptation. Additionally, the 5-fold cross-validation was incorporated further to ensure the stability of the estimate and reduce overfitting. The obtained results, as demonstrated in Table 4, confirm that the ML model can reliably anticipate device behavior and provide insights for performance optimization of the PSC device.[81,82]

The ML model yielded an average R^2 = 0.9635, MAE = 0.4506, and RMSE = 0.6253 across all output parameters as summarized in Table 4. The scatter plots assessing SCAPS simulated data and ML-predicted values for each parameter displayed in Fig. 15a–d indicate that most data points closely follow the diagonal line. This outcome ensures strong correlation between simulated and predicted values, supporting the high precision of the proposed lead-free PSC predictive framework.

3.12.2 Feature importance analysis. We considered nine different input parameters in the ML model as illustrated in Fig. 16 and 17. The feature importance and SHAP analysis based on the input parameters confirm the trustworthiness and consistency of the model.[83,84] The results reveal that operating temperature, along with top and bottom AL properties (thickness, doping, and defect levels), have the highest impact on device performance, where HTL and ETL doping contribute to a lesser extent. High absorber defects increase trap-assisted recombination, lowering carrier lifetime, FF, and J_{sc}. Elevated temperature accelerates non-radiative recombination and ion migration, impacting V_{oc} and stability. Additionally, interfacial properties of the ETL/absorber and HTL/absorber affect ion migration and recombination. These effects emphasize why absorber properties and temperature are key drivers of device performance, providing a clear physical basis for the ML predictions. Thus, the analysis validates the model's accuracy and provides guidance for the targeted development and optimization of the proposed lead-free DAPSC model.

3.12.3 Correlation matrix of input and output parameters. Pearson correlation matrix analysis, as depicted in Fig. 18, offers key insights into how physical parameters affect photovoltaic performance. It is noticed that the bottom AL thickness moderately improves PCE (+0.33) while its defect density negatively affects performance (−0.37), highlighting the fact of defect reduction in efficiency improvement. The V_{oc} shows a strong positive influence on PCE (+0.73) and FF (+0.88), while it is negatively affected by bottom AL defect density (−0.36). Similarly, J_{sc} correlates positively with PCE and FF, and its relationship with bottom AL thickness (+0.55) underscores the

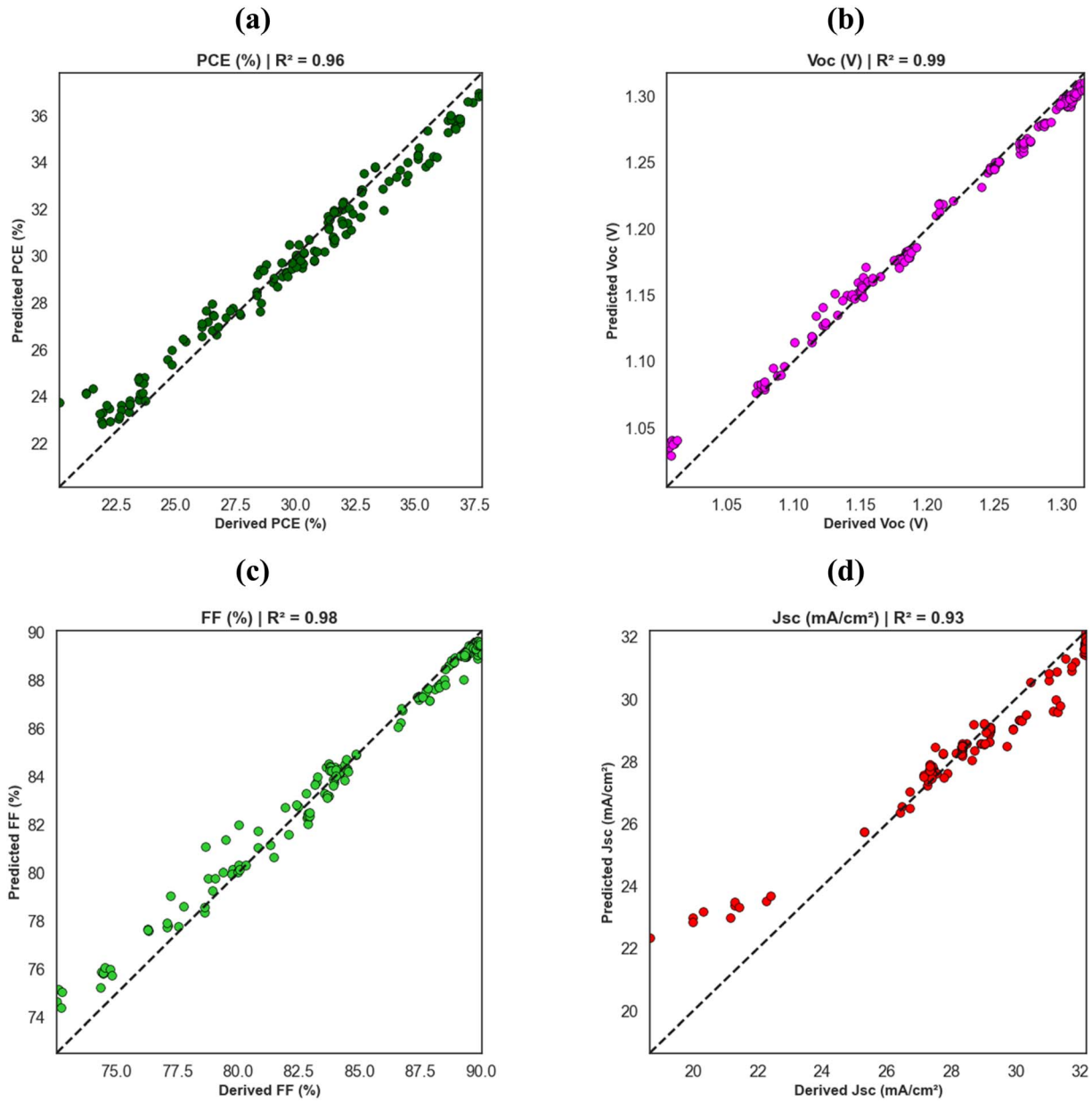

Fig. 15 Prediction accuracy of the proposed lead-free DAPSC model PCE (a), V_{oc} (b), FF (c), and J_{sc} (d).

importance of optimizing the absorber layer. Conversely, top AL thickness, top AL doping, and ETL donor density offer negligible impact, suggesting limited influence in this device structure. So, this correlation analysis of the optimized lead-free DAPSC model identifies key parameters that need to be prioritized for enhancing device performance.[85]

4. Limitations and future scope of the proposed PSC

While the dual-absorber lead-free PSCs exhibit encouraging simulated performance, some aspects remain to be explored experimentally. The outcomes of this study are based on idealized SCAPS-1D simulations; real device fabrication may reveal additional challenges such as interface imperfections and environmental impacts. However, multilayer and tandem perovskite devices have been successfully fabricated employing techniques such as orthogonal solvent selection, sequential deposition, interlayer engineering, and vapor-phase deposition to prevent layer mixing while maintaining enhanced charge transport.[86–88] These fabrication procedures create a credible pathway for constructing dual-absorber PSCs, establishing the applicability of our proposed dual-absorber PSC framework. Additionally, the RFR model, although effective for this dataset, may not generalize to other materials or device architectures. Future work should include experimental validation, exploration of advanced ML approaches such as neural networks, and

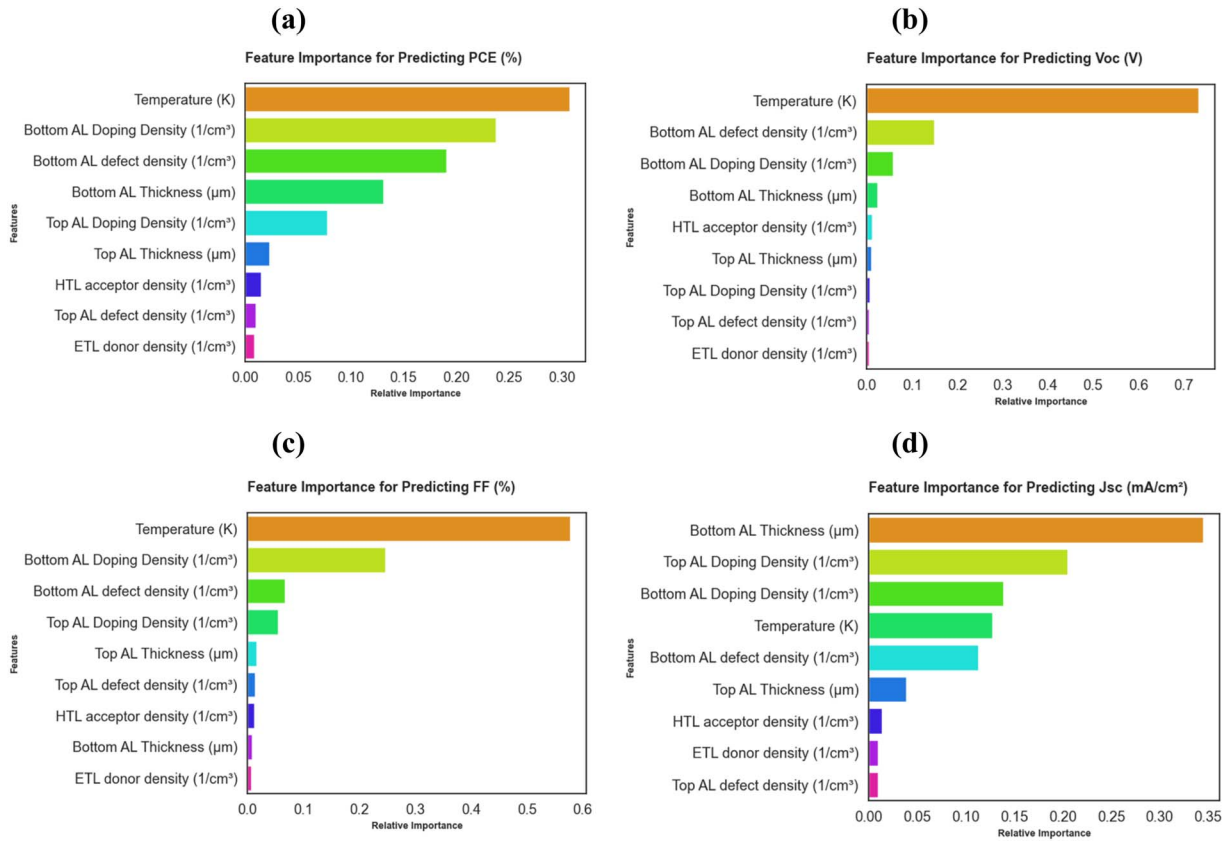

Fig. 16 Feature contributions to the predictive model for the proposed DAPSC: (a) PCE, (b) V_{oc}, (c) FF, and (d) J_{sc}.

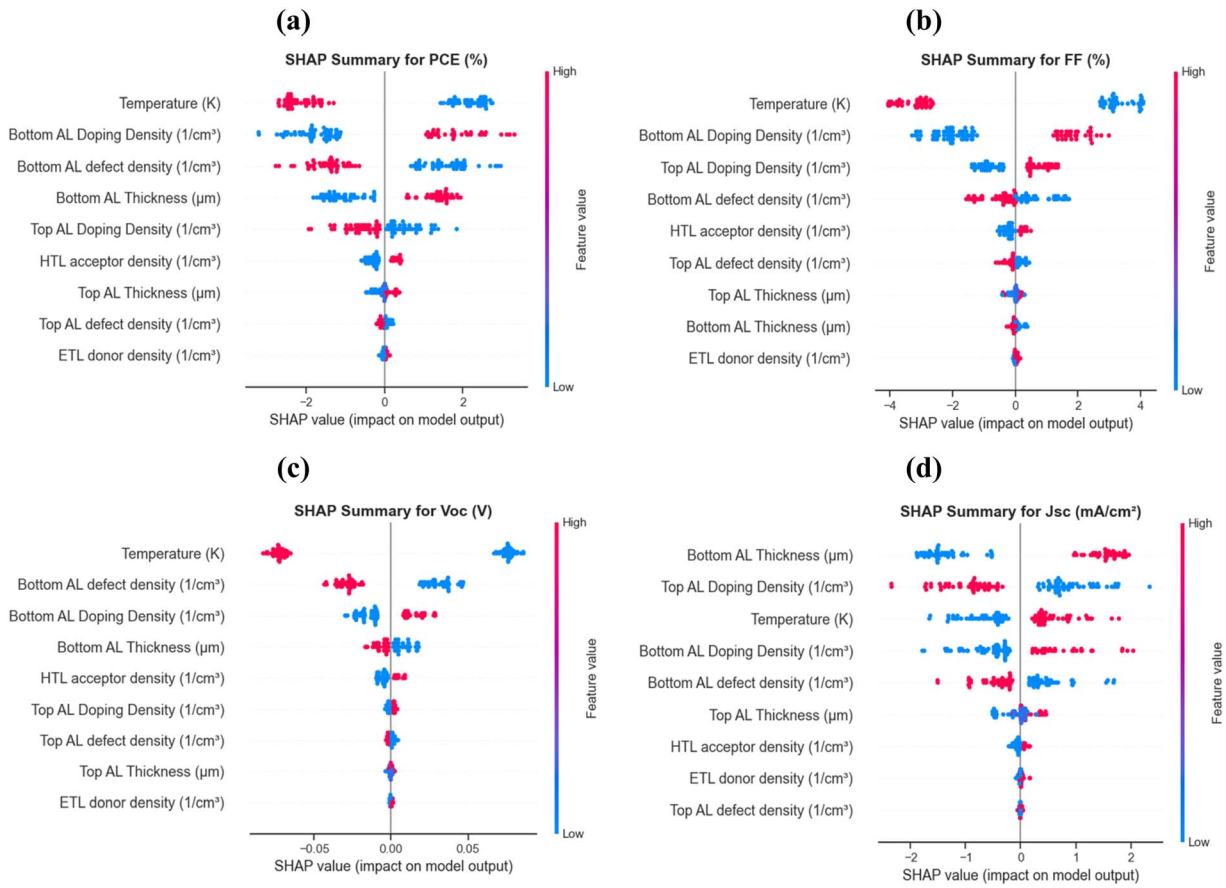

Fig. 17 SHAP analysis showing feature contributions to the predictive model of the optimized lead-free DAPSC: (a) PCE, (b) FF, (c) V_{oc}, and (d) J_{sc}.

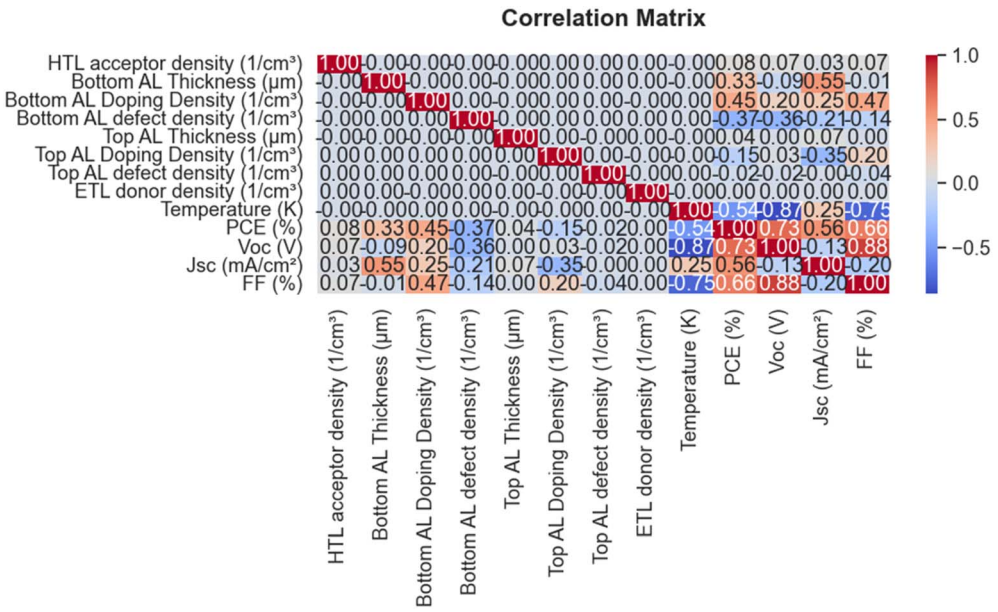

Fig. 18 Pearson correlation matrix of the proposed DAPSC configuration.

interface engineering to further enhance the performance, stability, and scalability of the lead-free dual-absorber PSCs.

5. Conclusion

This study introduces a novel design, extensive investigation, and performance optimization of inorganic halide lead-free dual-absorber Al/FTO/SnS_2/Ca_3SbI_3/Ba_3SbI_3/CBTS/Au-based PSC. The proposed optimized DAPSC structure consists of Ca_3SbI_3-based top absorber layer (with 1000 nm thickness and 1×10^{16} cm^{-3} doping concentration) and Ba_3SbI_3-based bottom absorber layer (with 300 nm thickness and 1×10^{18} cm^{-3} doping concentration). SCAPS-1D simulations reveal that the proposed optimized DAPSC design demonstrates performance advancement compared to single-absorber devices, achieving a peak PCE of 36.03%, V_{oc} of 1.305 V, J_{sc} of 32.18 mA cm^{-2}, and FF of 85.84%. Parametric studies elucidated that device operating temperature, absorber layer thickness, doping, and defect density are critical determinants of device performance, while ETL and HTL properties, interface defects, and series/shunt resistances also influence stability and performance. The RFR-based machine learning model supported accurate prediction of photovoltaic performance with an average R^2 of 0.9635, MAE of 0.4506, and RMSE of 0.6253, providing a promising framework for optimizing the proposed dual-absorber, lead-free PSCs. So, this study exhibits that M_3SbI_3-based DAPSC offers a promising route toward effective, reliable, and eco-friendly, sustainable photovoltaic applications.

Conflicts of interest

The authors declare the absence of any financial or personal interests that can bias the reported findings.

Data availability

The data will be available on a reasonable request.

Acknowledgements

The authors thank Dr Marc Burgelman as well as his group at Ghent University for allowing the SCAPS-1D simulation package to be used free of charge.

References

1 N. Kannan and D. Vakeesan, Solar energy for future world: - a review, *Renew. Sustain. Energy Rev.*, 2016, **62**, 1092–1105, DOI: 10.1016/j.rser.2016.05.022.
2 A. Siddique, M. N. Islam, A. A. M. Khan, H. Karmaker, M. A. Islam, A. K. M. A. Iqbal and B. K. Das, Numerical modelling and performance investigation of inorganic Copper-Tin-Sulfide (CTS) based perovskite solar cell with SCAPS-1D, *Results Opt.*, 2024, **8**, 100713, DOI: 10.1016/j.rio.2024.1007133.
3 R. A. Afre and D. Pugliese, Perovskite Solar Cells: A Review of the Latest Advances in Materials, Fabrication Techniques, and Stability Enhancement Strategies, *Micromachines*, 2024, **15**, 192.
4 S. Banik, A. Das, B. K. Das and N. Islam, Numerical simulation and performance optimization of a lead-free inorganic perovskite solar cell using SCAPS-1D, *Heliyon*, 2024, **10**(1), e23985, DOI: 10.1016/j.heliyon.2024.e23985.
5 V. Fthenakis, J. E. Mason and K. Zweibel, The technical, geographical, and economic feasibility for solar energy to supply the energy needs of the US, *Energy Policy*, 2009, **37**, 387–399, DOI: 10.1016/j.enpol.2008.08.011.

6 M. Z. Jacobson and M. A. Delucchi, A path to sustainable energy by 2030, *Sci. Am.*, 2009, **301**, 58–65, DOI: 10.1038/scientificamerican1109-58.
7 T. Ahmed, F. Rayhan, I. Rahaman, M. H. Rahman, M. M. H. Bappy, T. Ahammed and S. Ghosh, Optimization of buffer layers for CZTSSe solar cells through advanced numerical modelling, *J. Phys. Chem. Solids*, 2025, **204**, 112744, DOI: 10.1016/j.jpcs.2025.112744.
8 M. A. Green, E. D. Dunlop, M. Yoshita, N. Kopidakis, K. Bothe, G. Siefer, X. Hao and J. Jiang, Solar Cell Efficiency Tables (Version 65), *Prog. Photovolt. Res. Appl.*, 2025, **33**(1), 3–15, DOI: 10.1002/pip.3867.
9 A. Ghosh, *et al.*, Inorganic novel cubic halide perovskite Sr3AsI3: Strain-activated electronic and optical properties, *Heliyon*, 2023, **9**(8), e19271, DOI: 10.1016/J.HELIYON.2023.E19271.
10 M. F. Rahman, N. Mahmud, I. Alam, M. H. Ali, M. M. A. Moon, A. Kuddus, G. F. I. Toki, M. H. K. Rubel, M. A. Al Asad and M. K. Hossain, Design and numerical analysis of CIGS-based solar cell with V 2 O 5 as the BSF layer to enhance photovoltaic performance, *AIP Adv.*, 2023, **13**, 045309, DOI: 10.1063/5.0138354.
11 A. Isha, A. Kowsar, A. Kuddus, M. K. Hossain, M. H. Ali, M. D. Haque and M. F. Rahman, High efficiency Cu2MnSnS4 thin film solar cells with SnS BSF and CdS ETL layers: a numerical simulation, *Heliyon*, 2023, **9**, e15716, DOI: 10.1016/j.heliyon.2023.e15716.
12 M. F. Rahman, M. M. Alam Moon, M. K. Hossain, M. H. Ali, M. D. Haque, A. Kuddus, J. Hossain and A. B. Abu, Concurrent investigation of antimony chalcogenide (Sb2Se3 and Sb2S3)-based solar cells with a potential WS2 electron transport layer, *Heliyon*, 2022, **8**, e12034, DOI: 10.1016/j.heliyon.2022.e12034.
13 A. Kojima, K. Teshima, Y. Shirai and T. Miyasaka, Organometal halide perovskites as visible-light sensitizers for photovoltaic cells, *J. Am. Chem. Soc.*, 2009, **131**, 6050–6051, DOI: 10.1021/ja809598r.
14 S. D. Stranks, G. E. Eperon, G. Grancini, *et al*) Electron hole diffusion lengths exceeding 1 micrometer in an organometal trihalide perovskite absorber, *Science*, 2013, **342**, 341–344, DOI: 10.1126/science.1243982.
15 M. E. Ali, M. M. Haque and S. H. Cheragee, Device modeling and numerical analysis of lead-free $MASnI_3/Ca_3AsI_3$ based perovskite solar cells with over 38% efficiency, *Sol. Energy*, 2025, **288**, 113309, DOI: 10.1016/j.solener.2025.113309.
16 Q. Jiang, *et al.*, Surface passivation of perovskite film for efficient solar cells, *Nat. Photonics*, 2019, **13**(7), 460–466, DOI: 10.1038/s41566-019-0398-2.
17 Q. Fatima, A. A. Haidry, H. Zhang, A. El Jery and M. Aldrdery, A critical review on advancement and challenges in using TiO_2 as electron transport layer for perovskite solar cell, *Mater. Today Sustain.*, 2024, 100857, DOI: 10.1016/j.mtsust.2024.100857.
18 T. R. Cook, D. K. Dogutan, S. Y. Reece, *et al*) Solar energy supply and storage for the legacy and nonlegacy worlds, *Chem. Rev.*, 2010, **110**, 6474–6502, DOI: 10.1021/cr100246c.
19 X. Huang, D. Ji, H. Fuchs, *et al*) Recent progress inorganic phototransistors: semiconductor materials, device structures and optoelectronic applications, *ChemPhotoChem*, 2020, **4**, 9–38, DOI: 10.1002/cptc.201900198.
20 S. Bouazizi, *et al.*, Growth and efficiency of MAPbBr3 based perovskite solar cells: insight from experimental and simulation, *Indian J. Phys.*, 2024, **98**(9), 3341–3353, DOI: 10.1007/S12648-023-03065-4/FIGURES/13.
21 Y. Raoui, H. Ez-Zahraouy, N. Tahiri, O. El Bounagui, S. Ahmad and S. Kazim, Performance analysis of MAPbI3 based perovskite solar cells employing diverse charge selective contacts: simulation study, *Sol. Energy*, 2019, **193**, 948–955, DOI: 10.1016/j.solener.2019.10.009.
22 J. Seo, T. Song, S. Rasool, S. Park and J. Y. Kim, An Overview of Lead, Tin, and Mixed Tin–Lead-Based ABI3 Perovskite Solar Cells, *Adv. Energy Sustain. Res.*, 2023, **4**(5), 2200160, DOI: 10.1002/AESR.202200160;JOURNAL:JOURNAL:26999412.
23 M. Haneef, S. Tahir, H. A. Mahmoud, A. Ali and A. Ashfaq, Optimizing lead-free MASnBr 3 perovskite solar cells for high-efficiency and long-term stability using graphene and advanced interface layers, *ACS Omega*, 2024, **9**(6), 7053–7060, DOI: 10.1021/acsomega.3c08981.
24 P. Panda, S. Beriha and S. K. Tripathy, Design of MASnI3 perovskite solar cell with chalcogenide ETLs to achieve high photo conversion efficiency of 31.51% using SETFOS, *Optik*, 2024, **296**, 171550, DOI: 10.1016/j.ijleo.2023.171550.
25 W.-J. Yin, T. Shi and Y. Yan, Unique properties of halide perovskites as possible origins of the superior solar cell performance, *Adv. Mater.*, 2014, **26**, 4653–4658, DOI: 10.1002/adma.201306281[15].
26 W. Zhang, G. E. Eperon and H. J. Snaith, Metal halide perovskites for energy applications, *Nat. Energy*, 2016, **1**(6), 1–8.
27 G. E. Eperon, S. D. Stranks, C. Menelaou, *et al*) Forma midinium lead trihalide: a broadly tunable perovskite for efficient planar heterojunction solar cells, *Energy Environ. Sci.*, 2014, **7**, 982–988, DOI: 10.1039/c3ee43822h.
28 M. Petrović, V. Chellappan and S. Ramakrishna, Perovskites: Solar cells & engineering applications—materials and device developments, *Sol. Energy*, 2015, **122**, 678–699, DOI: 10.1016/j.solener.2015.09.041.
29 M. S. Reza, M. F. Rahman and A. Kuddus, Boosting efficiency above 28% using effective charge transport layer with Sr_3SbI_3-based novel inorganic perovskite, *RSC Adv.*, 2023, **13**, 31330–31345, DOI: 10.1039/d3ra06137j.
30 F. Rahman, R. Islam and A. Ghosh, Exploring the impact of strain on the electronic and optical properties of inor ganic novel cubic perovskite Sr3PI3, *Phys. Scr.*, 2023, **98**, 115105, DOI: 10.1088/1402-4896/acfce9.
31 A. Ghosh, M. F. Rahman, A. Kuddus and A. Irfan, Investigating of novel inorganic cubic perovskites of A_3BX_3 (A = Ca, Sr, B = P, As, X = I, Br) and their photovoltaic performance with efficiency over 28%, *J. Alloys Compd.*, 2024, **986**, 174097, DOI: 10.1016/j.jallcom.2024.174097.

32 I. K. G. Apurba, M. R. Islam, R. Khan, M. R. U. Nasib, M. F. Rahman, F. I. Bakhsh, A. Zahid and S. Ahmad, The density function theory analysis of the inorganic perovskite materials Mg_3AsX_3 (X = I, Br, Cl, and F): alteration of the physical properties by strain effect, *Mater. Sci. Semicond. Process.*, 2024, **183**, 108741, DOI: 10.1016/j.mssp.2024.108741.

33 M. Harun-Or-Rashid, *et al.*, Analysis of the role of A-cations in lead-free A3SbI3 (A = Ba, Sr, Ca) perovskite solar cells, *J. Mater. Sci.*, 2024, **59**(15), 6365–6385, DOI: 10.1007/S10853-024-09579-4/METRICS.

34 M. Ferdous Rahman, *et al.*, Boosting efficiency above 30% of novel inorganic Ba3SbI3 perovskite solar cells with potential ZnS electron transport layer (ETL), *Mater. Sci. Eng., B*, 2024, **300**, 117073, DOI: 10.1016/J.MSEB.2023.117073.

35 S. H. Cheragee and M. J. Alam, Device modeling and numerical study of a double absorber solar cell using a variety of electron transport materials, *Sol. Energy*, 2025, **258**, 112–123, DOI: 10.1016/j.heliyon.2023.e18265.

36 W. Farooq, T. Alshahrani, S. A. A. Kazmi, J. Iqbal, H. A. Khan, M. Khan, A. A. Raja and A. ur Rehman, Materials Optimization for thin-film copper indium gallium selenide (CIGS) solar cell based on distributed braggs reflector, *Optik*, 2021, **227**, DOI: 10.1016/j.ijleo.2020.165987.

37 M. A. Shafi, L. Khan, S. Ullah, M. Y. Shafi, A. Bouich, H. Ullah and B. Mari, Novel compositional engineering for ~26% efficient CZTS-perovskite tandem solar cell, *Optik*, 2022, **253**, DOI: 10.1016/j.ijleo.2022.168568.

38 D. L. Cocke, G. K. Chuah, N. Kruse and J. H. Block, Copper Oxidation and Surface Copper Oxide Stability Investigated by Pulsed Field Desorption Mass Spectrometry, *Appl. Surf. Sci.*, 1995, **84**, 153–161, DOI: 10.1016/0169-4332(94)00467-6.

39 J. Ge and Y. Yan, Synthesis and characterization of photoelectrochemical and photovoltaic Cu_2BaSnS_4 thin films and solar cells, *J. Mater. Chem. C*, 2017, **5**, 6406–6419, DOI: 10.1039/c7tc01678f.

40 C. Zhu, Y. Liu, D. Wang, Z. Zhu, P. Zhou, Y. Tu, G. Yang, H. Chen, Y. Zang, J. Du and W. Yan, Exploration of highly stable and highly efficient new lead-free halide perovskite solar cells by machine learning, *Cell Rep. Phys. Sci.*, 2024, **5**(12), 102321, DOI: 10.1016/j.xcrp.2024.102321.

41 J. Li, B. Pradhan, S. Gaur and J. Thomas, Predictions and strategies learned from machine learning to develop high performing perovskite solar cells, *Adv. Energy Mater.*, 2019, **9**(46), 1901891, DOI: 10.1002/aenm.201901891.

42 T. Zhang, J. Li, S. Wang, *et al.*, Ion-modulated radical doping of spiro-OMeTAD for more efficient and stable perovskite solar cells, *Science*, 2022, **377**(6605), 495–501, DOI: 10.1126/science.abo2757.

43 H. Huang, X. Liu, M. Wang, *et al.*, 24.8%-efficient planar perovskite solar cells via ligand-engineered TiO2 deposition, *Joule*, 2022, **6**(9), 2186–2202, DOI: 10.1016/j.joule.2022.07.004.

44 V. Krishnapressad, S. S. Parui and R. Ramesh Babu, Efficiency enhancement via novel lead-free inorganic $CsSnBr_3/Cs_3Bi_2I_9$ heterojunction absorber layer in perovskite solar cell, *Solid State Commun.*, 2025, **399**, 115888, DOI: 10.1016/j.ssc.2025.115888.

45 M. Burgelman, P. Nollet and S. Degrave, Modelling polycrystalline semiconductor solar cells, *Thin Solid Films*, 2000, **361–362**, 527–532.

46 M. Burgelman, K. Decock, S. Khelifi and A. Abass, Advanced electrical simulation of thin film solar cells, *Thin Solid Films*, 2013, **535**, 296–301.

47 M. A. Islam, A. Jawad, N. A. Jahan and M. M. Hossain, Outstanding conversion efficiency of 38.39% from a perovskite/CIGS tandem PV cell: A synergic optimization through computational modeling, *Heliyon*, 2023, **9**(10), e20558, DOI: 10.1016/j.heliyon.2023.e20558.

48 Y. H. Khattak, F. Baig, H. Toura, S. Ullah, B. Marí, S. Beg and H. Ullah, Effect of Cu_2O hole transport layer and improved minority carrier life time on the efficiency enhancement of Cu_2NiSnS_4 based experimental solar cell, *Curr. Appl. Phys.*, 2018, **18**, 633.

49 S. Sharbati, E. Norouzzadeh and S. Mohammadi, A simulation study to improve the efficiency of $ZnO_{1-x}S_x/Cu_2ZnSn(S_y, Se_{1-y})_4$ solar cells by composition-ratio control, *Opt. Mater.*, 2018, **78**, 259.

50 D. Srinivasan, A. R. Chettiar, K. T. Arockiadoss and L. Marasamy, A new class of $SrHfSe_3$ chalcogenide perovskite solar cells with diverse HTMs: Theoretical modelling towards efficiency enhancement, *Sol. Energy Mater. Sol. Cells*, 2025, **290**, 113727, DOI: 10.1016/j.solmat.2025.113727.

51 D. Sharma, R. Mehra and B. Raj, *Mathematical Modelling and Simulation of CH3NH3Pb(I1-Xbrx)3 Based Perovskite Solar Cells for High Efficiency*, 2021.

52 M. K. Hossain, G. F. I. Toki, I. Alam, R. Pandey, D. P. Samajdar, M. F. Rahman, M. R. Islam, M. H. K. Rubel, H. Bencherif, J. Madan and M. K. A. Mohammed, *New J. Chem.*, 2023, **47**, 4801.

53 M. K. Hossain, *et al.*, An extensive study on multiple ETL and HTL layers to design and simulation of high-performance lead-free CsSnCl3-based perovskite solar cells, *Sci. Rep.*, 2023, **13**(1), 1–24, DOI: 10.1038/s41598-023-28506-2.

54 Md. M. Islam, Md. F. Rahman, Md. H. Rahman, M. Z. Bani-Fwaz, R. Pandey and Md. Harun-Or-Rashid, Unlocking the Lead-Free New All-Inorganic Cubic Halide Perovskites of Ba_3MI_3 (M = P, As, Sb) with Efficiency above 29%, *J. Mater. Sci.*, 2024, **59**, 22109–22131, DOI: 10.1007/s10853-024-10487-w.

55 M. Hasanzadeh Azar, *et al.*, SCAPS Empowered Machine Learning Modelling of Perovskite Solar Cells: Predictive Design of Active Layer and Hole Transport Materials, *Photonics*, 2023, **10**, 271, DOI: 10.3390/PHOTONICS10030271.

56 F. Pedregosa, *et al.*, Scikit-learn: Machine Learning in Python, *J. Mach. Learn. Res.*, 2012, **12**, 2825–2830.

57 Md. S. Islam, Md. T. Islam, S. Sarker, H. Al Jame, S. S. Nishat, Md. R. Jani, A. Rauf, S. Ahsan, K. Md. Shorowordi, H. Efstathiadis, J. Carbonara and S. Ahmed, Machine learning approach to delineate the impact of material

properties on solar cell device physics, *ACS Omega*, 2022, **7**, 22263, DOI: 10.1021/acsomega.2c01076.

58 A. Maoucha, T. Berghout, F. Djeffal and H. Ferhati, Machine learning-guided analysis of CIGS solar cell efficiency: Deep learning classification and feature importance evaluation, *Sol. Energy*, 2025, **287**, 113251, DOI: 10.1016/j.solener.2025.113251.

59 F. Schmitz, Improved hole extraction and band alignment via interface modification, *Sol. RRL*, 2024, **8**, 2300965, DOI: 10.1002/solr.202300965.

60 S. He, B. Wang, P. Wang, Y. Wang, Y. Cheng, Y. Lv and Y. Li, Interfacial defects passivation and energy level alignment with small molecule pyridine material for efficient and stable inverted perovskite solar cells, *Surf. Interfaces*, 2024, **46**, 104031, DOI: 10.1016/j.surfin.2024.104031.

61 H. M. El-Hageen, A. N. Z. Rashed, H. Albalawi, M. A. Alhartomi, Y. H. Alfaifi, M. T. Alsubaie and M. A. Mead, Performance signature of the best candidate-graded bandgap materials for solar cells with steady-state conversion efficiency, *Energies*, 2023, **16**(19), 7001, DOI: 10.3390/en16197001.

62 T. B. Dev, A. Srivani, S. Rajpoot and S. Dhar, Novel lead-free dual absorber based perovskite solar cells: efficient numerical harnessing towards high efficiency through SCAPS-1D, *J. Phys. Chem. Solids*, 2025, **205**, 112776, DOI: 10.1016/j.jpcs.2025.112776.

63 S. M. Hasnain, I. Qasim, A. Iqbal, M. A. Mir and N. Abu-Libdeh, Novel dual absorber configuration for eco-friendly perovskite solar cells: design, numerical investigations and performance of ITO-C60-MASnI3-RbGeI3-Cu2O-Au, *Sol. Energy*, 2024, **278**, 112788, DOI: 10.1016/j.solener.2024.112788.

64 L. R. Karna, R. Upadhyay and A. Ghosh, All-inorganic perovskite photovoltaics for power conversion efficiency of 31%, *Sci. Rep.*, 2023, 1315212.

65 S. Ahmmed, M. A. Karim, M. H. Rahman, A. Aktar, M. R. Islam, A. Islam, Md Bakar and A. Ismail, Performance analysis of lead-free CsBi3I10-based perovskite solar cell through the numerical calculation, *Sol. Energy*, 2021, **226**, 54–63, DOI: 10.1016/j.solener.2021.07.076.

66 N. Singh, A. Agarwal and M. Agarwal, Numerical simulation of highly efficient lead-free all-perovskite tandem solar cell, *Sol. Energy*, 2020, **208**, 399–410, DOI: 10.1016/j.solener.2020.08.003.

67 Y.-N. Zhang, B. Li, L. Fu, Y. Zou, Q. Li and L.-W. Yin, Enhanced optical absorption and efficient cascade electron extraction based on energy band alignment double absorbers perovskite solar cells, *Sol. Energy Mater. Sol. Cells*, 2019, **194**, 168–176, DOI: 10.1016/j.solmat.2019.02.014.

68 F. Li, S. Zhou, J. Yuan, C. Qin, Y. Yang, J. Shi, X. Ling, Y. Li and W. Ma, *ACS Energy Lett.*, 2019, **4**, 2571.

69 M. Rahman, M. Habib, M. Ali, M. Rubel, M. R. Islam, A. B. M. Ismail and M. K. Hossain, *AIP Adv.*, 2022, **12**, 105317, DOI: 10.1063/5.0108459.

70 L.-J. Chen, C.-R. Lee, Y.-J. Chuang, Z.-H. Wu and C. Chen, Synthesis and Optical Properties of Lead-Free Cesium Tin Halide Perovskite Quantum Rods with High-Performance Solar Cell Application, *J. Phys. Chem. Lett.*, 2016, **7**(24), 5028–5035, DOI: 10.1021/acs.jpclett.6b02344.

71 S. Islam, D. D. Ria, M. M. Mia, M. K. A. Mohammed, M. F. Hossain, A. Irfan, N. Dhahri and M. F. Rahman, Introducing a new and highly efficient double-absorber solar cell with combination of Sr_3PBr_3 and $CsPbI_3$ perovskites, *Phys. Status Solidi A*, 2025, **222**(19), 2500148, DOI: 10.1002/pssa.202500148.

72 A. Ghosha, N. Lal Deyb, M. Rafid Hasanc, M. Aliahsan Bappyd, M. Humaun Kabire, S. Begumf, S. Ahmedg, A. Salam Howladere, N. S. Awwadh and H. A. Alturaifih, Innovative double absorber solar cell design combining Ca3AsI3 and Ca3PI3 perovskites for achieving over 29% efficiency, *Opt. Laser Technol.*, 2025, **183**, 112399, DOI: 10.1016/j.optlastec.2024.112399.

73 M. F. Rahman, M. Rahman, M. F. Hossain, B. Islam, S. R. Al Ahmed and A. Irfan, A Numerical Strategy for Achieving Efficiency Exceeding 32% with a Novel Lead-Free Dual-Absorber Solar Cell Using Ca3SbI3 and Sr3SbI3 Perovskites, *Adv. Photonics Res.*, 2025, **6**(5), 2400148, DOI: 10.1002/ADPR.202400148.

74 S. H. Cheragee, J. A. Akhi, M. Dev, M. Haque, M. A. Kabir, T. Hossain, M. T. Alam and M. J. Alam, Optimized non-toxic double absorber perovskite solar cell with efficiency beyond 33%, *Results Opt.*, 2025, **19**, 100813, DOI: 10.1016/j.rio.2025.100813.

75 S. Khatoon, S. K. Yadav, J. Singh and R. B. Singh, Design of a $CH_3NH_3PbI_3$/$CsPbI_3$-based bilayer solar cell using device simulation, *Heliyon*, 2022, **8**(7), e09941, DOI: 10.1016/j.heliyon.2022.e09941.

76 N. Hui, T. Sanyal, and R. Das, A brief review on solar photovoltaic: A key to sustainable development, in *A Basic Overview of Environment and Sustainable Development*, IAPH, 2024, Vol. 3, 3rd edn, Chapter 8. doi: DOI: 10.52756/boesd.2024.e03.008.

77 B. Farhadi, J. You, D. Zheng, L. Liu, S. Wu, J. Li, *et al.*, Machine learning for fast development of advanced energy materials, *Next Mater.*, 2023, **1**(3), 100025, DOI: 10.1016/j.nxmate.2023.100025.

78 K. Prakash, A. James, N. J. Valeti and M. K. Singha, Optimization and numerical studies with machine learning assisted graphene-based $CuSbS_2$ thin film solar cell for flexible electronics applications, *J. Phys. Chem. Solids*, 2025, **199**, 112513, DOI: 10.1016/j.jpcs.2024.112513.

79 A. Ghosh, A. S. Zishan, M. Moumita, Y. A. Kumar, A. K. Roy, S. Islam, *et al.*, Improving the performance of $AgCdF_3$-based perovskite solar cells using machine learning-driven adjustment of active layer and charge transport materials with SCAPS-1D, *Inorg. Chem. Commun.*, 2025, **179**(Part 2), 114829, DOI: 10.1016/j.inoche.2025.114829.

80 I. Chabri, M. Said, E. El-Allaly and A. Oubelkacem, Machine learning-assisted SCAPS device simulation for photovoltaic parameters prediction of perovskite solar cells, *Mater.*

Today Commun., 2024, **41**, 110585, DOI: 10.1016/j.mtcomm.2024.110585.

81 J. Hu, Z. Chen, Y. Chen, H. Liu, W. Li, Y. Wang, L. Peng, X. Liu, J. Lin, X. Chen and J. Wu, Interpretable machine learning predictions for efficient perovskite solar cell development, *Sol. Energy Mater. Sol. Cells*, 2024, **271**, 112826, DOI: 10.1016/j.solmat.2024.112826.

82 M. Saqib, U. Shoukat, M. M. Soliman, S. Bashir, M. H. Tahir, H. K. Thabet and M. Kallel, Machine learning assisted designing of hole-transporting materials for high performance perovskite solar cells, *Chem. Phys.*, 2025, **589**, 112515, DOI: 10.1016/j.chemphys.2024.112515.

83 S. Subba and S. Chatterjee, Machine learning-driven determination of key absorber layer parameters in perovskite solar cells, *Mater. Today Commun.*, 2025, **42**, 111113, DOI: 10.1016/j.mtcomm.2024.111113.

84 I. I. Malek, H. Imtiaz and S. Subrina, Machine learning driven performance enhancement of perovskite solar cells with CNT as both hole transport layer and back contact, *Sol. Energy*, 2024, **278**, 112737, DOI: 10.1016/j.solener.2024.112737.

85 M. F. Rahman, M. H. Rahman, M. R. Islam, *et al.*, The optical and electronic properties of inorganic halide perovskite Sr3NCl3 under applied biaxial strain, *J. Mater. Sci.*, 2023, **58**, 13100–13117, DOI: 10.1007/s10853-023-08825-5.

86 D. P. McMeekin, S. Mahesh, N. K. Noel, M. T. Klug, J. Lim, J. H. Warby, J. M. Ball, L. M. Herz, M. B. Johnston and H. J. Snaith, Solution-Processed All-Perovskite Multi-junction Solar Cells, *Joule*, 2019, **3**(2), 387–401.

87 S.-H. Huang, C.-T. Tsou, Y.-H. Hsiao, C.-F. Li, Y.-R. Chen, W.-F. Su and Y.-C. Huang, High-Efficiency Perovskite Solar Cell with an Air-Processable Active Layer via Sequential Deposition, *Mater. Sustain.*, 2025, **1**(1), 3, DOI: 10.53941/matsus.2025.100003.

88 Y. Yao, S. Liu, C. D. Rodríguez-Gallegos, *et al.*, Perovskite-based multi-junction solar cells, *Nat. Rev. Clean Technol.*, 2025, **1**, 771–787, DOI: 10.1038/s44359-025-00103-8.